Asian Journal of Electrical and Electronic Engineering

VOLUME 2 ISSUE 2 SEPTEMBER 2022

AlamBiblio Publishers
ESTB: 2020
003160938-P

eISSN 2785-8189
9 772785 818002

https://alambiblio.com/ojs/index.php/ajoeee

ASIAN JOURNAL OF ELECTRICAL AND ELECTRONIC ENGINEERING

COPYRIGHT NOTICE

Consent to publish: The Author(s) agree to publish their articles with AlamBiblio Press.

Declaration: The Author(s) declare that the article has not been published before in any form. It is not concurrently submitted to another publication and does not infringe on anyone's copyright. The author (s) holds the AlamBiblio Press and Editors of the Journal harmless against all copyright claims.

Transfer of copyright: The Author(s) hereby agree to transfer the article's copyright to **AlamBiblio Press**, which shall have the non-exclusive and unlimited right to publish the article in any form, including in electronic media. For articles with more than one author, the corresponding author confirms that he/she is authorized by his/her co-author(s) to grant this transfer of copyright.

The Asian Journal of Electrical and Electronic Engineering Journal follows the open access policy.

All articles published with open access will be immediately and permanently free for everyone to read, download, copy and distribute.

ASIAN JOURNAL OF ELECTRICAL AND ELECTRONIC ENGINEERING

eISSN 2785-8189

9 7 7 2 7 8 5 8 1 8 0 0 2

Published by:

AlamBiblio Press,
PV8 platinum Hill
Jalan Melati Utama, 53100 Kuala Lumpur, Malaysia
Phone (+603) 2713 7308

Whilst the publisher and editorial board make every effort to see that no inaccurate or misleading data, opinion or statement appears in this Journal, they wish to make it clear that the data and opinions appearing in the articles and advertisements herein are the responsibility of the contributor or advertiser concerned. Accordingly, the publisher and the editorial committee accept no liability whatsoever for the consequence of any such inaccurate or misleading data, opinion or statement.

This work is licensed under a Creative Commons Attribution-Non-Commercial 4.0 International License.

ASIAN JOURNAL OF ELECTRICAL AND ELECTRONIC ENGINEERING

AIMS & SCOPE OF THE ASIAN JOURNAL OF ELECTRICAL AND ELECTRONIC ENGINEERING

The **Asian Journal of Electrical and Electronic Engineering** (**AJoEEE**), published biannually (March and September), is a peer-reviewed open-access journal of the **AlamBiblio Press**.

The Asian Journal of Electrical and Electronic Engineering publishes original research findings as regular papers and review papers (by invitation). The Journal provides a platform for Engineers, Researchers, Academicians, and Practitioners who are highly motivated to contribute to the Electrical and Electronics Engineering disciplines. It also welcomes contributions that address the developing world's specific challenges and address science and technology issues from a multidisciplinary perspective.

REFEREES' NETWORK

All papers submitted to AJoEEE Journal will be subjected to a rigorous reviewing process through a worldwide network of specialized and competent referees. Each accepted paper should have at least two positive referees' assessments.

SUBMISSION OF A MANUSCRIPT

A manuscript should be submitted online to the Asian Journal of Electrical and Electronic Engineering (AJoEEE) website https://alambiblio.com/ojs/index.php/ajoeee. Further correspondence on the status of the paper could be done through the journal website

Volume 2, Issue 2, September 2022

TABLE OF CONTENTS

ARTICLES

ASIAN JOURNAL OF ELECTRICAL AND ELECTRONIC ENGINEERING
Vol. 2 No. 2 2022
E-ISSN: 2785-8189

A New Topology of High-Efficiency DC-DC Hybrid Boost SEPIC Converter for PV Cell

Khadiza Akter, S. M. A. Motakabber, AHM Zahirul Alam, Siti Hajar Yusoff

Dept. of Electrical and Computer Engineering,
International Islamic University,
Kuala Lumpur, Malaysia

*Corresponding author: amotakabber@iium.edu.my

(Received: 5th July 2022; Accepted: 6th September 2022)

Abstract— This paper initiates a high-gain high efficiency step-up DC-DC converter based on Boost SEPIC (Single Ended Primary Inductor Converter) hybrid topology for photovoltaic application. Customarily DC-DC converter circuit is a widely used technique to improve the voltage level of solar cells. However, for low output voltage and low efficiency, they are not sufficient enough to provide expected outcomes. To defeat the conventional system a hybrid Boost SEPIC topology has been recommended with enhanced performance. The proposed design of the DC-DC converter circuit can provide a high voltage gain without decaying its overall performance. The modified converter topology is being worked by a single switch with low switching voltage stress over the semiconductor devices. The main edge of the proposed design is that it can perform efficiently without using any transformer, the combined design of Boost SEPIC topology increases the voltage gain much higher compared to the conventional Boost or SEPIC. The maximum Power Point Tracking (MPPT) algorithm is used to obtain maximum power from a photovoltaic source. MATLAB Simulink and PSIM software has analyzed the performance of the newly designed converter circuit thoroughly.

Keywords: *Step-up Converter, High voltage gain, SMPS, MOSFET Switch*

1. INTRODUCTION

In recent years, the fast ascent in power demand and the change in biological circumstances, for example, the rise of worldwide temperature by using traditional sources, for example, consumption of oil and coal brings about the developing greenhouse impact and contamination issues in the environment. It expands the need for novel assets of energy, which is modest and increasingly maintainable. Due to several reasons, the use of renewable energy is highly increased as clean and sustainable energy. From the available resources of renewable energy, solar energy is the biggest contributor to clean emission-free and inexpensive energy [1]. For the increasing demand for renewable energy systems, photovoltaic systems and semiconductors, the industry requires wide use of high-efficiency DC-DC power electronic converters. The output voltage levels from these sources are commonly low and unregulated and it doesn't coordinate with the load and should be expanded [2]. The most feasible and efficient way to increase the low voltage of a PV array and reduce the voltage strains on semiconductor components, according to several researchers, is to use high step-up DC-DC converters [3]. The easiest architectures for achieving a high-voltage gain are cascaded and multilayer converters, however because of the numerous stages and numerous power switches, they have low efficiency [4]. The output voltage of a PV cell usually ranges from 12 V to 50 V. Inherently DC-DC step-up converter is used for increasing the voltage level and output gain of solar energy [5]. Fig.1 Present a PV system where A DC-DC step-up converter is used to increase the output voltage of the PV source, which can be converted again to an AC output through an inverter to the load [6].

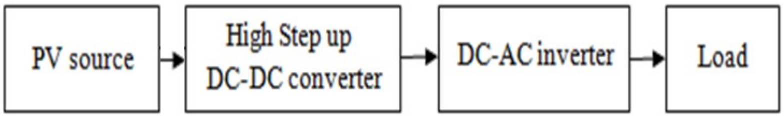

Fig. 1. Basic step-up of a photovoltaic system

A high-frequency transformer can build the desired output however it has a certain disadvantage of leakage current due to the inductance of the transformer [7]. Nevertheless, to improve productivity, just as diminish the absolute leakage current, the converter without a transformer is examined throughout this research. Over the years, several solutions and topologies have been proposed by researchers for the improvement of the overall power quality of DC-DC converters, however, most of them suffer from low gain and low efficiency [2], [7]–[12]. The proposed topology introduces a hybrid DC-DC converter with a solitary switch. Topology consolidates two traditional DC-DC converters to improve the output gain without interfacing a mid-point transformer [13].

The conventional DC-DC converter experiences some power losses like losses in MOSFET, input & output capacitance loss, diode loss, inductor losses etc. The total power losses in a boost converter are the sum of all factors. In the case of SEPIC, similar difficulties are seen and the inductor and capacitor resistance affect the efficiency and output ripple [5]. DC-DC boost converter system is useful to increase the output voltage level. Due to the leakage resistance of the inductor, the performance of the conductor decreases with the increasing duty cycle ratio of the switch. Therefore, a traditional boost converter cannot be used for high voltage requirements [6]. The convergence of this paper is firstly to build up a DC-DC converter with a mix of boost and SEPIC together. It has significant merits such as high voltage gain and high efficiency which makes this design a good choice to be implemented. Additionally, the altered converter has been contrasted and different sorts of converters dependent on similar parameters and has been analyzed the performance of the adjusted boost SEPIC converter. The control of the proposed converter is simple because a single switch is utilized.

This paper is sectionalized into five sections. Section I of this article has described the background of conventional non-isolated DC-DC converters along with their limitation while connected with a photovoltaic system. The modelling and operation of the proposed circuit are described in section II. Section III is explaining the theoretical analysis of the ideal voltage gain of the proposed converter. Simulation result analyses have been broadly discussed in sections IV and V accordingly.

2. MODELLING OF MODIFIED BOOST-SEPIC CONVERTER

The proposed circuit that appeared in Fig. 2 is formed by the Boost converter and SEPIC converter. The major primacy of this converter is to lessen the number of switches and inductors contrasted with the other existing isolated converters. For the most part, the voltage stress over the switch is in addition diminished alongside the decrease in input current ripple. The boost converter has the advantage of high step-up voltage gain whereas the SEPIC converter has the merits of continuous input and output current. The proper combination of both topologies can enhance the overall performance of the desired parameter which can contribute to optimizing the performance of solar PV cells.

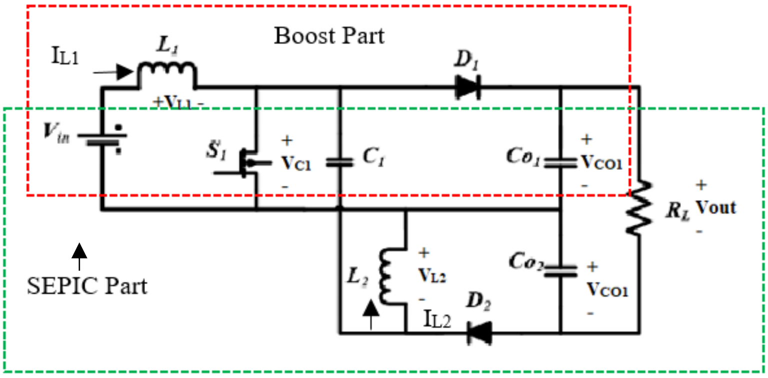

Fig. 2. Proposed DC-DC hybrid boost SEPIC converter

The principle of operation of the proposed hybrid circuit has been explained in Fig. 3 and 4 respectively. The circuit has used five passive elements and two diodes. A MOSFET is used as a switch. The circuit operation can be classified into two types based on the ON and OFF operation of the MOSFET switch. When the switch of S_1 is turned on, the diode D_1 does not direct for being reversely biased, in this way, consequently current in inductor L_1 will build up, thus capacitor C_{O1} and C_{O2} will be charged equally. The direction of current flow during switch ON mode is shown in Fig. 3.

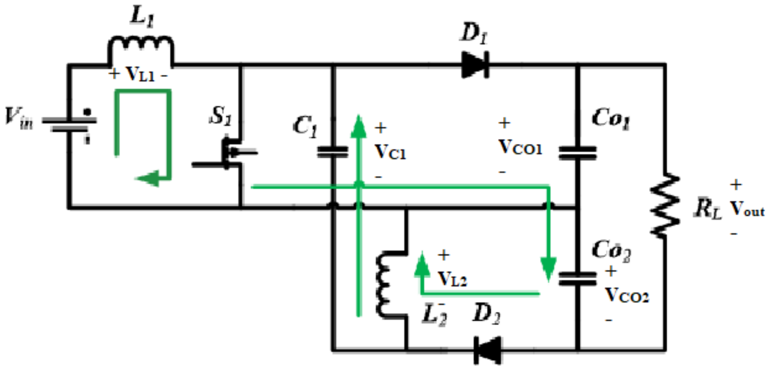

Fig. 3. Mode 1, currents in the circuit during switch ON

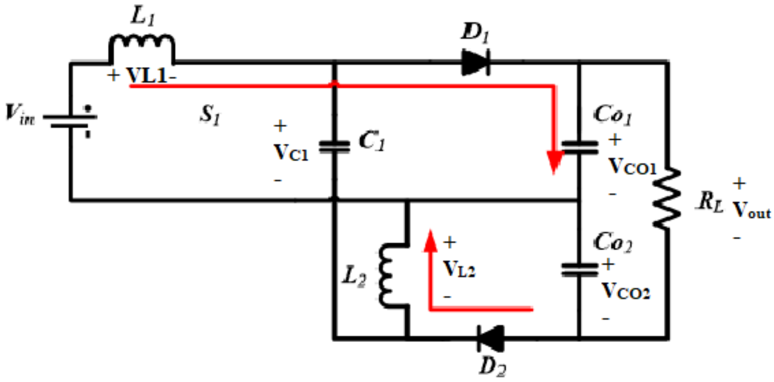

Fig. 4. Mode 2, currents in the circuit during switch OFF

When the MOSFET Switch S_1 is off; the Diode D_1 has led for its forward one-sided Voltage. An inductor will release its stored energy and the current will continue to flow as shown in Fig. 4. The simulation setup of the proposed circuit is depicted in Fig. 5 (a). Perturb and observe-based MPPT algorithm is used to obtain maximum power from the solar module. Fig. 5 (b) shows the block of MPPT to generate the desired duty cycle for pulse width modulation (PWM) of the MOSFET switch. Perturb and the observe-based algorithm is shown in Fig. 5 (c). The theoretical waveform of inductor current L_1 and L_2 during switch ON and OFF conditions is demonstrated in Fig. 6.

3. ANALYSIS OF PROPOSED HYBRID CONVERTER

In order to determine the voltage, and gain equation of the proposed converter all semiconductor components, capacitors and inductors are assumed to be ideal. The circuit is operating in continuous conduction mode at a steady state.

The voltage gain of the proposed hybrid converter circuit is calculated using the assumption that the inductors' steady-state average voltages V_{L1} and V_{L2} over one switching cycle is zero. applying Kirchhoff's voltage law, the voltage drop across the inductor from Fig. 3 and Fig. 4 for both modes of operation is given in Eq. (1) and Eq. (3) respectively.

$$\int_0^{T_s} V_{L1}(t)dt = D_{Ts}V_{in} + [(1-D)T_s](V_{in} - V_{CO1}) \tag{1}$$

Where D is the duty cycle ratio of the MOSFET switch and T_s is the switching period. The duty cycle can be calculated using the following equation.

$$D = \frac{T_{ON}}{T_s} \tag{2}$$

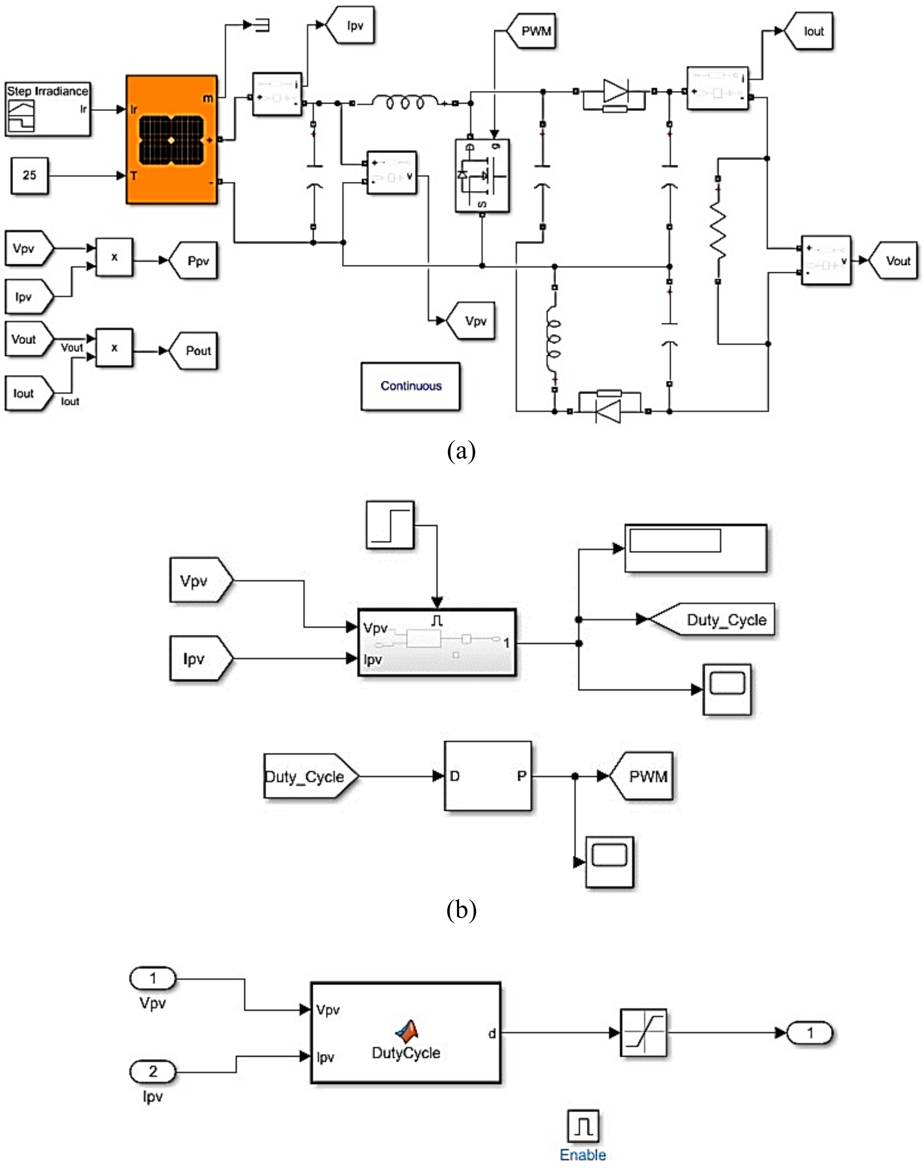

(a)

(b)

(c)

Fig. 5. (a) Simulation setup in Simulink, (b) Block diagram of MPPT controller (c) Perturb and observe algorithm block

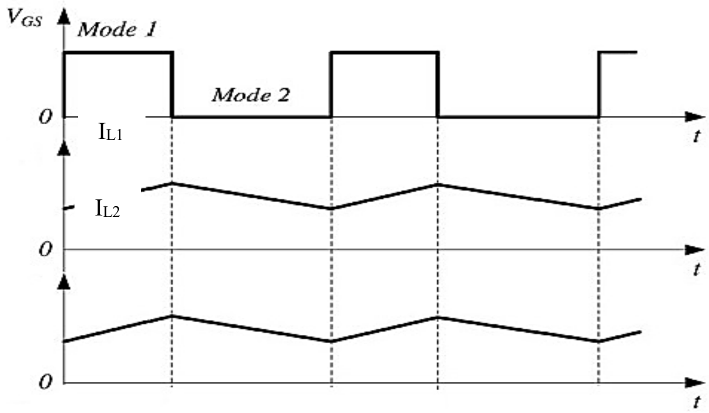

Fig. 6. Voltage and current waveform in different modes

Since voltage in the second balance, over one switching cycle is zero. The voltage across capacitor C1 can be calculated using Eq. 1.

$$V_{CO1} = \frac{V_{in}}{1-D} \tag{3}$$

Apply volt second balance theorem on L_2 over one switching cycle we will get

$$\int_0^{T_s} V_{L2}(t)dt = D_{Ts}(V_{in} - V_{CO2}) + (1-D)T_sV_{CO2} \tag{4}$$

Solving Eq. 4, voltage across capacitor C2 can be written as,

$$V_{CO2} = \left(\frac{D}{1-2D}\right)V_{in} \tag{5}$$

The net output voltage of the circuit can be calculated as,

$$V_{out} = V_{CO1} + V_{CO2} \tag{6}$$

Putting Eq. 4 and Eq. 5 in Eq. 6 to calculate the voltage gain

$$G_V = \frac{V_{out}}{V_{in}} = \frac{(1-D)^2 + D}{(1-D)(1-2D)} \tag{7}$$

4. RESULT

The chosen value of the proposed circuit along with its performance is given in detail in this section. The analysis and simulation have progressed by using PSIM and Simulink software. Table I contains the values of the component which have been selected for simulation. Table II reveals the outstanding performance in terms of output voltage and efficiency of the proposed design compared to conventional design. During simulation, conventional converters and the hybrid Boost-SEPIC converter operate at the same input voltage (36V) and same switching frequency (20kHz) and same value parameter.

TABLE 1: SPECIFICATION OF CIRCUIT PARAMETERS

Parameter	Value
Capacitor (C_1)	470 uF
Capacitor ($Co_1 = Co_2$)	470 uF
Inductor (L_1= L_2)	4.7 mH
Load Resistor (R)	50 Ω
Switching Frequency (F)	20 kHz
Solar Irradiance	1000W/m^2
Temperature	25°
Photovoltaic Output Voltage	36V

TABLE II: EFFICIENCY AND OUTPUT VOLTAGE COMPARISON

Converters	Boost	SEPIC	Boost-SEPIC
Efficiency	94.83%	87.64 %	98.60%
Output Voltage	74V	38V	126 V

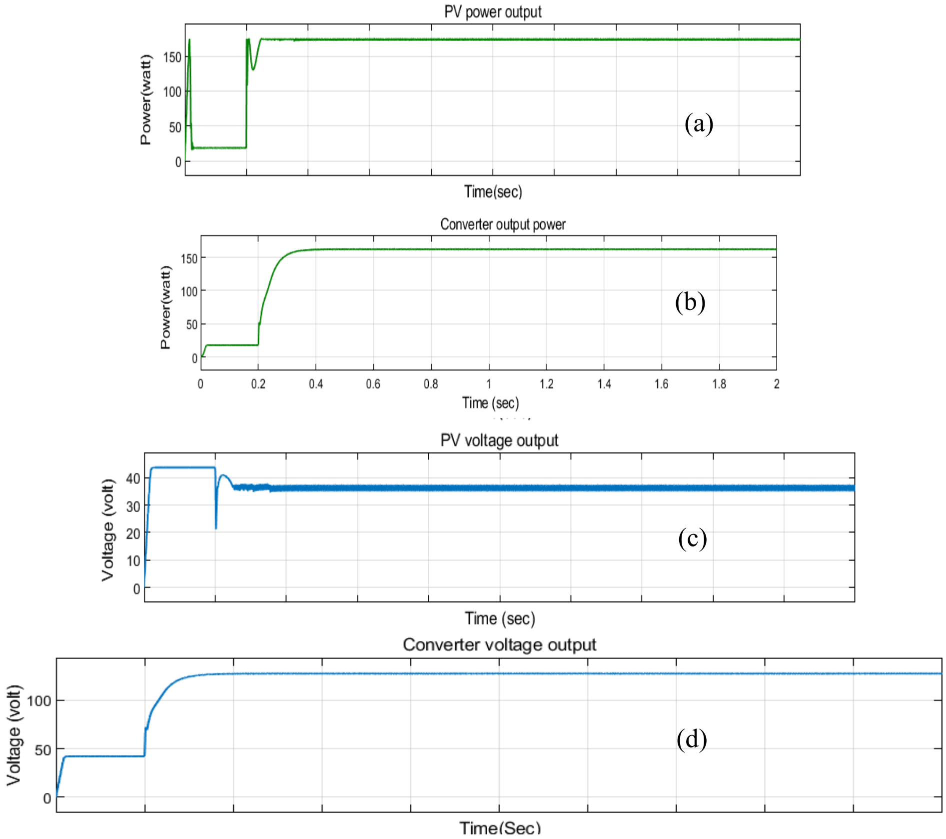

Fig. 7. Waveform of (a) PV Power output, (b) Converter power output, (c) PV voltage output and (d) Converter voltage output

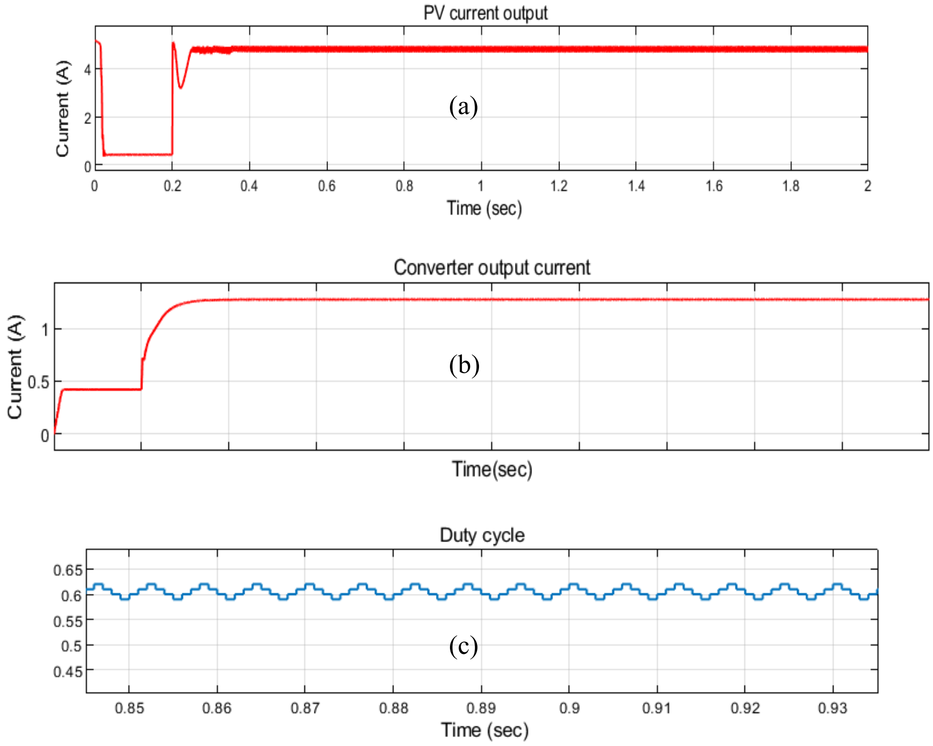

Fig. 8. Waveform, (a) PV current output, (b) Converter current output and (c) Duty cycle

TABLE 2: OUTPUT PERFORMANCE COMPARISON

CONVERTERS	BOOST	SEPIC	BOOST-SEPIC
EFFICIENCY	94.83%	87.64 %	98.60%
OUTPUT VOLTAGE	74V	38V	126 V

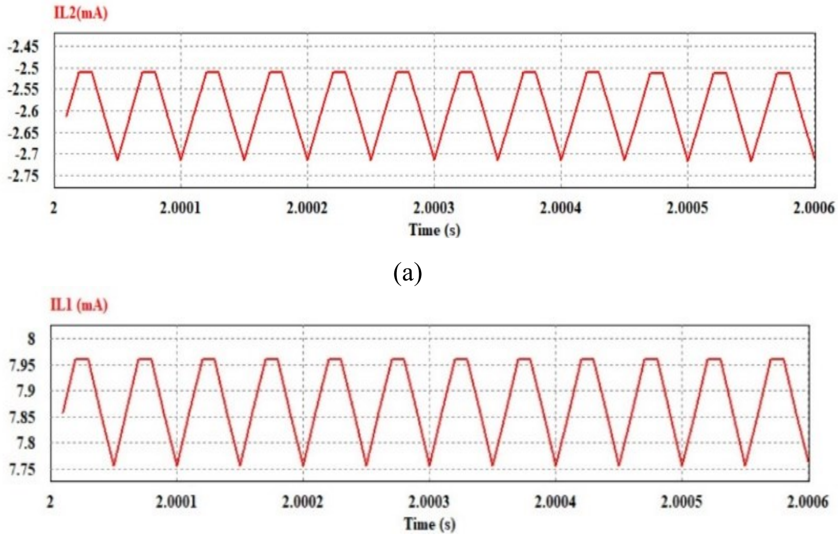

(a)

(b)

Fig. 9. Current waveform (a) Inductor L_1 and (b) Inductor L_2

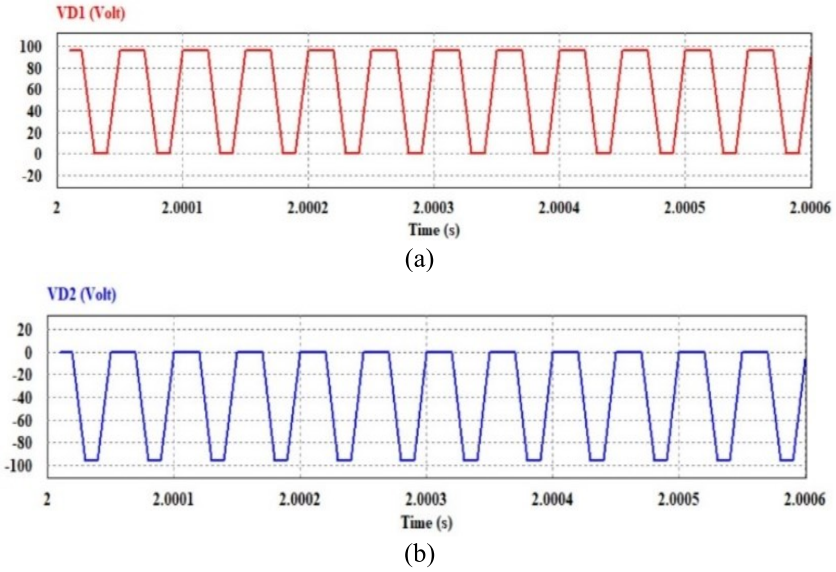

(a)

(b)

Fig. 10. Voltage waveform across diode, (a) D_1 and (b) D_2

5. RESULT ANALYSIS

Simulation results of conventional and proposed circuits are shown graphically in this section. Fig. 7 displays the waveform of PV and converter power and voltage output. It is understandable from the figures. that proposed hybrid model is performing significantly better. From Fig. 8(c) and Fig. 8(d) it is visible that the proposed circuit noticeably reduced the fluctuation of output voltage compared to input. Similarly, the converter output current also contains less ripple, which is shown in Fig. 9(b). Current flowing through inductors L1 and L2 in Fig. 10 has the same waveform at CCM similar to the theoretical waveform. Fig. 11 displays the efficiency of the conventional converter and proposed converter in the same parametric situation. It is visible from the graphical representation that the proposed circuit outperforms compared to other converter circuits in all possible manners throughout the variation of the duty cycle, which is depicted in Fig. 11.

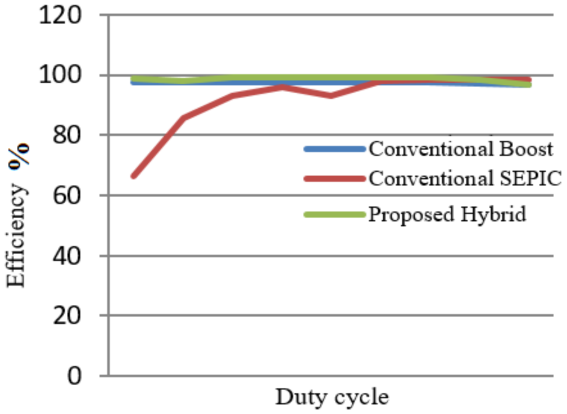

Fig. 11. Efficiency comparison of various converter

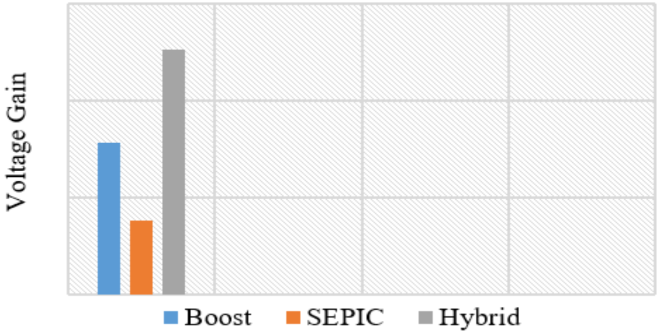

Fig. 12. Voltage gain of the conventional and proposed converter

Fig. 12 is indicating the voltage gain of the proposed converter is the highest among all other converter circuits. The proposed converter can perform efficiently for different values of loads and switching frequency, which have been shown in Fig. 14 and 15 respectively.

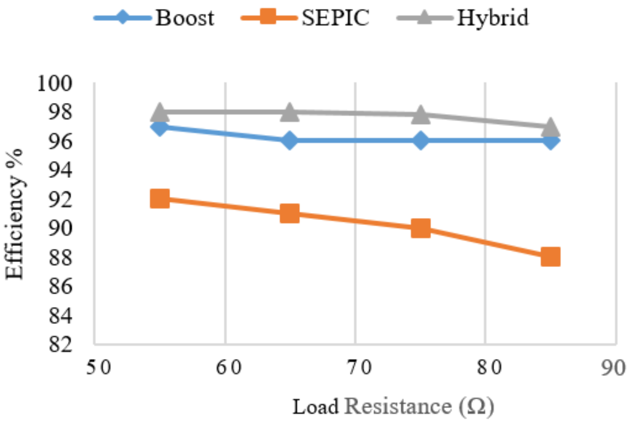

Fig. 13. Observation of efficiency under load variation

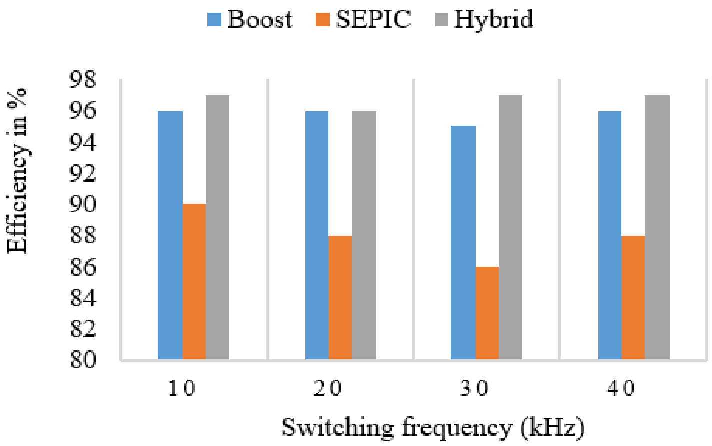

Fig. 14. Observation of efficiency under frequency variation

6. CONCLUSION

The analysis of the proposed hybrid Boost- SEPIC DC-DC converter depending on SMPS technology is carried out to boost the output voltage level of the photovoltaic cell. Surveying of the proposed design shows that the high voltage gains and continuous current conversion is possible to achieve without worsening the transformation efficiency. Besides that, the proposed circuit is also able to eliminate the switching and other circuit element stress. The performance of the converter has been simulated and tested under different parameters variation such as switching frequencies, duty cycle and load with the help of PSIM and Simulink software. From the result analysis, it is obvious that the recommended configuration is performing better than the existing configuration. The proposed converter demonstrated its capacity to meet solar source requirements by offering a high amplitude and efficiency of 98%.

REFERENCES

[1] S. Ali *et al.*, "Evaluating green technology strategies for the sustainable development of solar power projects: Evidence from Pakistan," *Sustain.*, vol. 13, no. 23, pp. 1–29, 2021, DOI: 10.3390/su132312997

[2] F. Mumtaz, N. Zaihar Yahaya, S. Tanzim Meraj, B. Singh, R. Kannan, and O. Ibrahim, "Review on non-isolated DC-DC converters and their control techniques for renewable energy applications," *Ain Shams Eng. J.*, vol. 12, no. 4, pp. 3747–3763, 2021, DOI: 10.1016/j.asej.2021.03.022

[3] A. Torkan and M. Ehsani, "A Novel Nonisolated Z-Source DC-DC Converter for Photovoltaic Applications," IEEE Trans. Ind. Appl., vol. 54, no. 5, pp. 4574–4583, 2018, DOI: 10.1109/TIA.2018.2833821

[4] S. Salehi, N. Zahedi, R. Kheirollahi, and E. Babaei, "Ultra High Step-up DC-DC Converter Based on Switched Inductor-Capacitor Cells," *2019 10th Int. Power Electron. Drive Syst. Technol. Conf. PEDSTC 2019*, pp. 367–372, 2019, DOI: 10.1109/PEDSTC.2019.8697841

[5] S. Poshtkouhi and O. Trescases, "Multi-input single-inductor DC-DC converter for MPPT in parallel-connected photovoltaic applications," Conf. Proc. - IEEE Appl. Power *Electron. Conf. Expo. - APEC*, vol. 4, pp. 41–47, 2011, DOI: 10.1109/APEC.2011.5744573

[6] K. Kanathipan, M. A. M. Cheema, and J. Lam, "Five-Level Inverter With A Combined DC Voltage Balancing and Fault-voltage Mitigation Technique for Grid-Connected PV Energy Systems," *2021 IEEE PES Innov. Smart Grid Technol. - Asia, ISGT Asia 2021*, 2021, DOI: 10.1109/ISGTASIA49270.2021.9715629

[7] E. Ragonese, N. Spina, A. Parisi, and G. Palmisano, "An experimental comparison of galvanically isolated dc-dc converters: Isolation technology and integration approach,"

Electron., vol. 10,no. 10, 2021, DOI: 10.3390/electronics10101186

[8] O. Kircioğlu, M. Ünlü, and S. Çamur, “Modeling and analysis of DC-DC SEPIC converter with coupled inductors,” *2016 Int. Symp. Ind. Electron. INDEL 2016 - Proc.*, 2016, DOI: 10.1109/INDEL.2016.7797807

[9] C. Muranda, E. Ozsoy, S. Padmanaban, M. S. Bhaskar, V. Fedák, and V. K. Ramachandaramurthy, “Modified SEPIC DC-to-DC boost converter with high output-gain configuration for renewable applications,” *2017 IEEE Conf. Energy Conversion, CENCON 2017*, vol. 2018-January, pp. 317–322, 2017, DOI: 10.1109/CENCON.2017.8262505

[10] K. S. Kavin and P. Subha Karuvelam, “PV-based Grid Interactive PMBLDC Electric Vehicle with High Gain Interleaved DC-DC SEPIC Converter,” *IETE J. Res.*, 2021, DOI: 10.1080/03772063.2021.1958070

[11] A. Mahmood *et al.*, “A Non-Inverting High Gain DC-DC Converter with Continuous Input Current,” *IEEE Access*, vol. 9, pp. 54710–54721, 2021, DOI: 10.1109/ACCESS.2021.3070554

[12] R. Rahimi, S. Habibi, P. Shamsi, and M. Ferdowsi, “A Dual-Switch Coupled Inductor-Based High Step-Up DC-DC Converter for Photovoltaic-Based Renewable Energy Applications,” pp. 1–6, 2021

[13] L. Yang, J. Peng, F. Yang, Y. Zhang, and H. Wu, “Single-Phase High-gain Bidirectional DC/AC Converter Based on High Step-up/step-down DC/DC Converter and Dual-input DC/AC Converter,” *PEDG 2019 - 2019 IEEE 10th Int. Symp. Power Electron. Distrib. Gener. Syst.*, pp. 554–559, 2019, DOI: 10.1109/PEDG.2019.8807762

ASIAN JOURNAL OF ELECTRICAL AND ELECTRONIC ENGINEERING
Vol. 2 No. 2 2022
E-ISSN: 2785-8189

Video-Based Vehicle Counting and Analysis using YOLOv5 and DeepSORT with Deployment on Jetson Nano

Abuelgasim Saadeldin*, Muhammad Mahbubur Rashid

Department of Mechatronics, Faculty of Engineering,
International Islamic University Malaysia,
Kuala Lumpur, Malaysia

*Corresponding author: ashaikh.saad.as@gmail.com

(Received: 12Th August 2022; Accepted: 28th August 2022)

Abstract— In recent years, the advancements in deep learning and high-performance edge-computing systems have increased tremendously and have become the center of attention when it comes to the analysis of video-based systems on edge by making use of computer vision techniques. Intelligent Transportation Systems (ITS) is one area where deep learning can be used for several tasks including highway-based vehicle counting systems whereby making use of computer vision techniques, an edge computing device and cameras installed in specific locations on the road, we are able to obtain very accurate vehicle counting results and replace the use of traditional and laborious hardware devices with modern low-cost solutions. This paper proposes and implements a modern, compact, and reliable vehicle counting system based on the most recent and popular object detection algorithm as of writing this paper, known as the YOLOv5, combined with a state-of-the-art object tracking algorithm known as DeepSORT. The YOLOv5 will be used in the following system to detect and classify four different classes of vehicles, whereas DeepSORT will be used to track those vehicles across different frames in the video sequence. Finally, a unique and efficient vehicle counting method will be implemented and used to count tracked vehicles across the highway scenes. A new highway vehicle dataset consisting of four vehicle classes, namely: car, motorcycle, bus, and truck, was collected, cleaned, and annotated with a total of 11,982 images published in the following study and used for the training of our robust vehicle detection model. From the results obtained over real-world highway surveillance videos, the following system was able to obtain an average vehicle detection mAP score of 96.1% and a vehicle counting accuracy of 95.39%, all while being able to be deployed on a compact Nvidia Jetson Nano edge-computing device with an average speed of 15 FPS which outperforms other previously proposed tools in terms of both accuracy and speed.

Keywords: *Vehicle Detection, Vehicle Tracking, Vehicle Counting, YOLOv5, Edge Deployment*

1. INTRODUCTION

In the past decade, the number of vehicles on the road has started to increase, leading to huge amounts of traffic congestion and various other safety concerns. The study of traffic flow analysis began to grow rapidly as researchers tried and identify ways of reducing congestion on the road by gathering essential information about moving vehicles required for developing better traffic management systems. In the past, physical hardware devices were placed underneath roadways and used to collect various data. Recently, with the advancements in technology and computer vision techniques, researchers began to actively look into vision-based solutions to help gather essential information required for maintaining constant traffic flows.

Vision-based solutions can provide us with more detailed information and are significantly easier to install and maintain compared to traditional physical hardware sensors. In this research, we will be making use of the current state-of-the-art object detection and tracking algorithms to develop a real-time highway-based vehicle counting system that will be low-cost, efficient and at the same time also compact enough to be deployed on low computationally expensive edge-computing devices. The YOLOv5, which is the most prominent object detection algorithm, will be used as the base model for the development of our custom vehicle detection algorithm; meanwhile, Simple Online and Realtime Tracking with a Deep Association Metric (DeepSORT) will be used for the tracking of vehicles across different frames in the video sequence. Finally, a unique and efficient counting method will be implemented to count tracked vehicles across the highway scenes.

2. METHODOLOGY

This section presents the methodology of our proposed vehicle counting system. It explains how it has been developed from data collection up to deployment and describes the environmental setup used for testing the following system. This section also elaborates on how the custom vehicle detection architecture was developed and how it has been integrated with a robust DeepSORT object tracking algorithm and a lightweight OSNet ReID model for tracking detected vehicles across different frames in the video sequence. Finally, we introduce a new and efficient vehicle counting method which will be used for counting different vehicle classes as they cross through a virtual polygon area on the highway in real-time.

2.1 System Architecture

Although a vast majority of vehicle counting systems have been implemented in the past, new advancements in the field of AI, object detection and tracking continue to emerge, introducing new features and significant improvements from one another. Fig. 1 below shows a summary of our proposed vehicle counting system, which was developed by utilizing a custom vehicle detection algorithm based on the YOLOv5, combined with a DeepSORT object tracking algorithm and a uniquely developed vehicle counting method. The system is comprised of three main components, which are vehicle detection, tracking, and counting. The vehicle detection will be used for the detection and classification of four different classes of vehicles, the vehicle tracking will be used for the vehicle ID assignment and tracking and finally the vehicle counter will be used for the counting of tracked vehicles as they cross through a virtual polygon area in the highway in real-time.

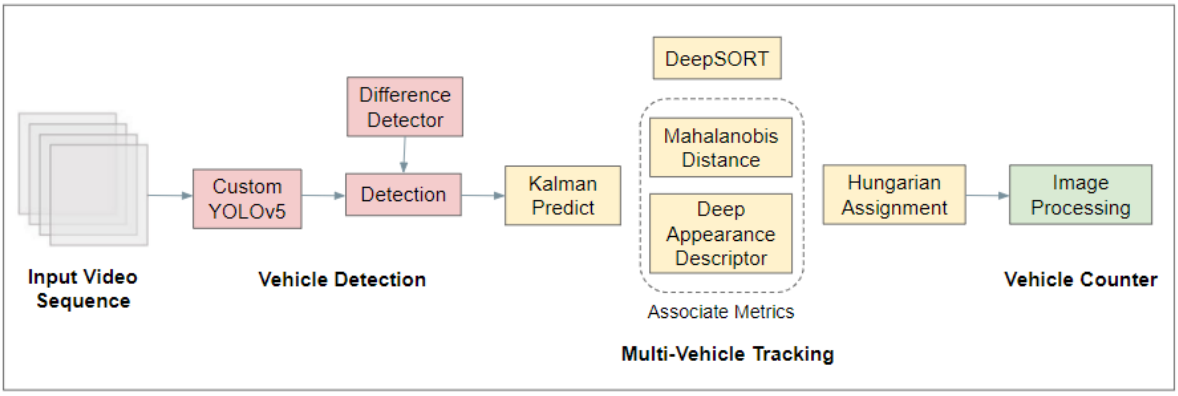

Fig. 1. Proposed System Architecture

2.2 Data Collection and Description

Highway traffic images from various sources, including open-source datasets, footages from CCTV cameras, and manually captured images, were the kinds of data used in this study. The main open-source datasets included the highway vehicle dataset [1] and MIO-TCD dataset [2]. The highway vehicle dataset is a large dataset containing vehicles captured from 23 surveillance cameras located in Hangzhou, China. Meanwhile, the MIO-TCD is a popular traffic dataset acquired from cameras deployed all over Canada and the United States. Open-source CCTV camera footage obtained from various locations at Shah Alam, Malaysia, was also dissected and used in the following dataset. Finally, manually captured images recorded by using a 12-megapixel smartphone camera situated on top of a pedestrian bridge and pointing directly towards a busy highway located in Kuala Lumpur, Malaysia was also utilized for generation of the vehicle dataset.

The generated vehicle dataset consists of four vehicle classes, namely: Car, Motorcycle, Bus, and Truck, which were captured from various locations, different timings throughout the day, varying weather conditions and have dramatic changes in scale, allowing for a robust model that is able to generalize well in different environments and weather conditions. The following dataset was annotated, exported in a YOLO text file format, and split into the train, valid and test sets with the following ratios 0.7, 0.2 and 0.1, respectively. Altogether 11,982 manually annotated images were generated and have been published at the following link: https://tinyurl.com/yc2eycje. In this dataset, cars accounted for 58.23%, motorcycles accounted for 7.35; buses accounted for 11.27% and trucks accounted for 23.15%. Table 1 shows detailed information about the generated dataset along with the number of instances for each of the four vehicle classes in each train, valid and test sets.

Table 1: Vehicle Dataset Information

Subset	Number of Images	Number of Cars	Number of Motorcycles	Number of Buses	Number of Trucks
All	11,982	23,360	1,950	2,975	9,286
Train	8,237	16,252	890	1,382	6,500
Validation	2,350	5,487	60	395	2,653
Test	1,184	2,336	45	198	929

2.2.1 Data Augmentation

Data augmentation was applied to the training images to increase the dataset's quality and allow for a highly generalizable model that can adapt to different environments and weather conditions. The data augmentation that was applied to the training images included the addition of random image rotations, adding noise, rain, and varying brightness, which resulted in an increase in the total number of training samples to 11,597 images, while the validation and test sets remained unchanged. Fig. 2 below shows a sample input image that has gone through the different augmentation techniques and the results are also displayed.

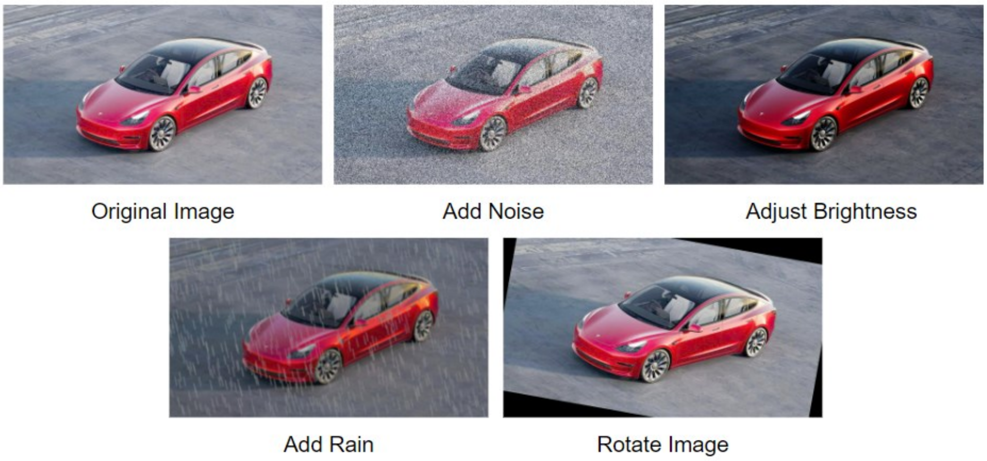

Fig. 2. Different Augmentations applied to Sample Image

2.3 Vehicle Detection

In this study, a CNN-based vehicle detection algorithm was developed and utilized. The algorithm is based on the YOLOv5 which is a popular object detection algorithm written in Python and which makes use of the PyTorch deep learning framework [3]. The YOLOv5 provides five different scales of their model, which are the Nano, Small, Medium, Large and Extra-large as shown in Fig. 3. The difference between each one of these scales is merely in the depth and width of the model which has been expanded, meaning that the overall structure of the model remains the same, however, the size and complexity of the model increases. The sample structures can also be modified by adding more neurons, increasing the number of hidden layers, and performing batch normalization or weight initialization. In our experiment, we made use of the smallest, fastest base model, the YOLOv5n and modified the structure by adding extra layers in order to improve the detection accuracy of smaller vehicle objects observed on highways while still maintaining a lightweight model able to be deployed on embedded devices.

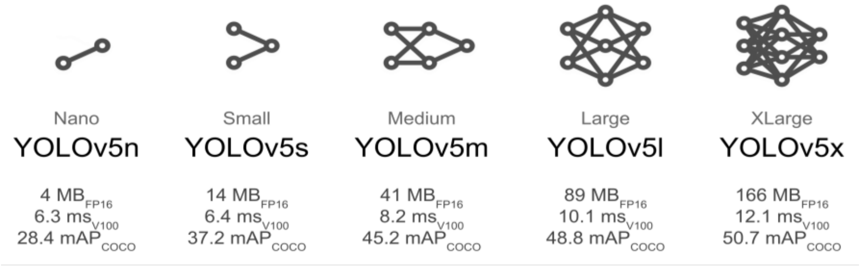

Fig. 3. The Different YOLOv5 Model Scales

The size of vehicles captured from a distance of approximately 5 meters above the ground can be relatively small. Therefore, accurately detecting the vehicles by using the default smallest YOLOv5n model architecture can be difficult. Hence, the addition of modules in order to increase the detection accuracy of smaller vehicle objects while still maintaining a fast and lightweight model is necessary. Thus, we have added an attention mechanism layer to the YOLOv5n model architecture along with additional up-sampling and down-sampling layers to the feature map in order to further improve the model's accuracy on smaller vehicle detections. The attention mechanism layer is a Convolutional Block Attention Module (CBAM) which replaces the original CONV module, allowing for more detailed information about passing vehicles by reducing the attention on roads and other complex backgrounds. Meanwhile, the up-sampling and down-sampling layers enhance the model's ability to detect vehicles at different scales and recognize different sizes and standards of the same vehicle. Fig. 4 below presents the improved model architecture where rows 12, 24-27 and 47-49 represent the replaced attention mechanism and additional small target detection layers, respectively.

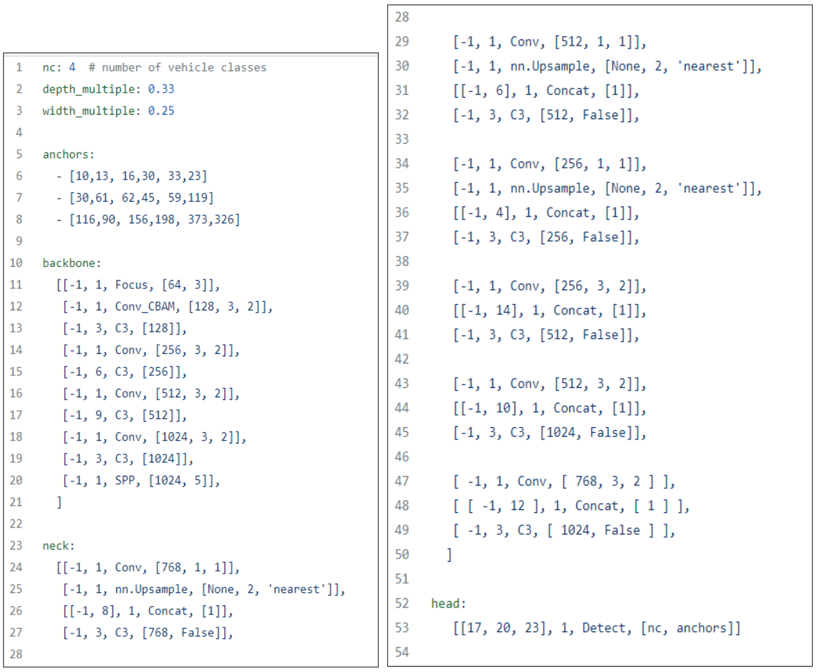

```
1   nc: 4  # number of vehicle classes
2   depth_multiple: 0.33
3   width_multiple: 0.25
4
5   anchors:
6     - [10,13, 16,30, 33,23]
7     - [30,61, 62,45, 59,119]
8     - [116,90, 156,198, 373,326]
9
10  backbone:
11    [[-1, 1, Focus, [64, 3]],
12     [-1, 1, Conv_CBAM, [128, 3, 2]],
13     [-1, 3, C3, [128]],
14     [-1, 1, Conv, [256, 3, 2]],
15     [-1, 6, C3, [256]],
16     [-1, 1, Conv, [512, 3, 2]],
17     [-1, 9, C3, [512]],
18     [-1, 1, Conv, [1024, 3, 2]],
19     [-1, 3, C3, [1024]],
20     [-1, 1, SPP, [1024, 5]],
21    ]
22
23  neck:
24    [[-1, 1, Conv, [768, 1, 1]],
25     [-1, 1, nn.Upsample, [None, 2, 'nearest']],
26     [[-1, 8], 1, Concat, [1]],
27     [-1, 3, C3, [768, False]],
28
```

```
28
29     [-1, 1, Conv, [512, 1, 1]],
30     [-1, 1, nn.Upsample, [None, 2, 'nearest']],
31     [[-1, 6], 1, Concat, [1]],
32     [-1, 3, C3, [512, False]],
33
34     [-1, 1, Conv, [256, 1, 1]],
35     [-1, 1, nn.Upsample, [None, 2, 'nearest']],
36     [[-1, 4], 1, Concat, [1]],
37     [-1, 3, C3, [256, False]],
38
39     [-1, 1, Conv, [256, 3, 2]],
40     [[-1, 14], 1, Concat, [1]],
41     [-1, 3, C3, [512, False]],
42
43     [-1, 1, Conv, [512, 3, 2]],
44     [[-1, 10], 1, Concat, [1]],
45     [-1, 3, C3, [1024, False]],
46
47     [ -1, 1, Conv, [ 768, 3, 2 ] ],
48     [ [ -1, 12 ], 1, Concat, [ 1 ] ],
49     [ -1, 3, C3, [ 1024, False ] ],
50    ]
51
52  head:
53     [[17, 20, 23], 1, Detect, [nc, anchors]]
54
```

Fig. 4. Proposed Vehicle Detection Model Architecture

In order to accurately detect small-scale vehicles captured on the highway scenes, after the focus module in the backbone network, an attention mechanism Conv_CBAM module is added which replaces the original CONV module. By doing so, the algorithm is able to obtain more detailed information about passing vehicles by reducing inference on roads and other complex backgrounds. The CBAM module pays attention to the channel information which solves the loss problem caused by the different weights in the feature graph. It works by taking the output of the channel attention module. It then goes through two pooling operations and a convolution operation with a convolution kernel of size 7x7. Finally, a feature graph with the size of HxWx2 is obtained. The main innovation in this network is in the addition of the CBAM and up-sampling and down-sampling layers which allowed for the model to learn the spatial attention features of vehicles through the relationship between channel and space.

2.4 Vehicle Tracking

Once the vehicles have been detected by using the custom YOLOv5 algorithm, vehicle features are then extracted and a DeepSORT multi-object tracking algorithm is used for the matching of features with the other video frames in order to achieve a correlation between the same vehicle and other similar vehicles. The DeepSORT algorithm works by using a combination of the Kalman Filter and Hungarian algorithm for tracking. The Kalman Filter is used for making a prediction of the current state of a vehicle based on some previous value, along with providing the uncertainties of that prediction [4]; a Mahalanobis distance is then used to encompass the uncertainties made by the Kalman Filter. Finally, once the vehicle location has been derived, the Hungarian algorithm is then used for the vehicle association and ID attribution, assigning a unique identification to the vehicle and identifying if the vehicle present in the current frame is the same as that observed in the previous frame [5]. The block diagram of the discussed flow of data in the DeepSORT algorithm can be seen in the Fig. 5.

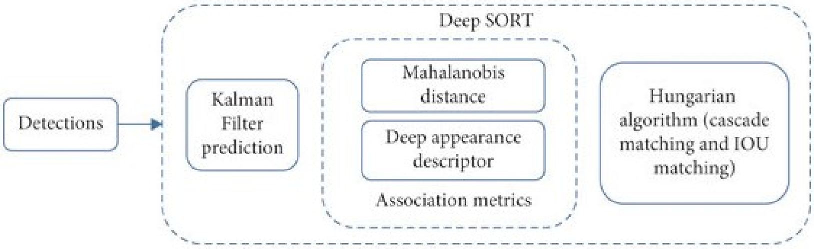

Fig. 5. Flow of Data in the DeepSORT algorithm [6]

The aim of the vehicle tracker is to be able to keep track of the detected vehicles and maintain their ID assignment as they move around in different frames in the video sequence. In order to accomplish this, we employed an Omni-Scale Network (OSNet) ReID model for the extraction of better representational feature vectors required for associating the vehicles in the highway scenes. OSNet specializes in multi-scale predictions and it designs its network with depth-wise separable convolutions, achieving an average mAP score of 84.9% on the Market 1501 dataset [7]. Furthermore, the combination of DeepSORT and OSNet ReID models is also lightweight, allowing for fast inference times and the ability to be deployed on edge-computing devices.

2.5 Vehicle Counting

Due to the very similar features observed in some vehicles, ID switches may occur from time to time during the tracking which may result in inaccurate vehicle counts. Therefore, in order to increase the robustness of the vehicle counter by not relying solely on the vehicle tracker and ID assignment for the counting, we introduced a "virtual polygon area" for accurately counting the total number of vehicles that have traveled across the highway. The virtual polygon area works by dividing the scenes into two areas, Zone 1 and Zone 2 as shown in Fig. 6. Zone 1 refers to the region that is located outside of the virtual polygon area, whereas Zone 2 refers to the region that is located within the specified polygon area. The user selects four points which will be used for drawing the virtual polygon area and the vehicle counting will be performed once the vehicles have crossed the highway and their center coordinates enter from Zone 1 into Zone 2 and the vehicle ID assignment remains unique.

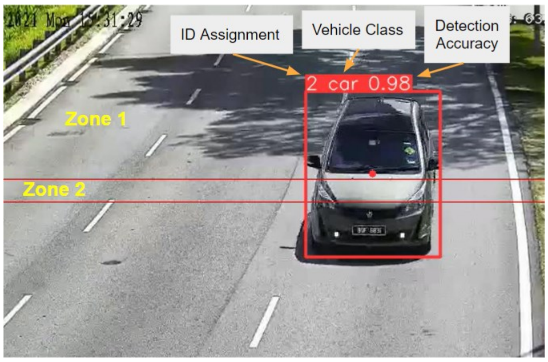

Fig. 6. Virtual Polygon Area used for Vehicle Counting

2.6 Model Deployment on Edge-Computing System

The Jetson Nano edge-computing device based on ARM architecture and produced by Nvidia was used for testing our vehicle counting system. The device is small, approximately 70 x 45 mm in size and brings in the performance of an efficient computer to the edge by use of a Single Board Computer (SBC). It is equipped with a Quad-core ARM Cortex-A57 CPU, 128 Nvidia CUDA Cores and 4GB of RAM with 64-bit LPDDR4 [8]. A Logitech C922 Pro HD Webcam, a 7-inch 1024 x 600 LCD Display and a portable 10,000mAh Mi Power bank were added to the device in order to form an edge-computing system platform. The flowchart used for counting the number of vehicles on the highway scenes is shown in Fig. 7. It works by firstly obtaining the video stream of the vehicles by using the Logitech webcam, and then the information is transmitted to the RAM of the edge-computing device. The Jetson Nano will then use this information as input and run inference of the vehicle detection, tracking, and counting. Finally, the output from the system will be the vehicle detection results as well as the number of vehicles that have crossed the highway shown separately for each of the vehicle classes on the 7” LCD display.

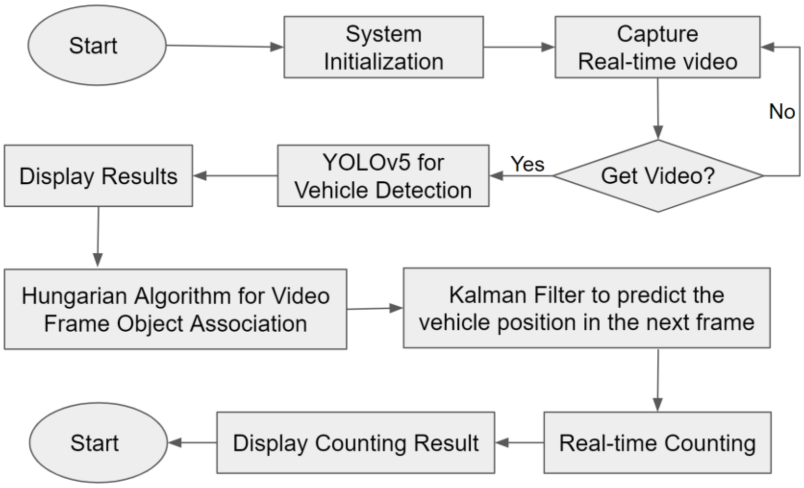

Fig. 7. Vehicle Counting System Flowchart

3. RESULTS AND DISCUSSION

This section presents the performance and evaluation of our proposed vehicle counting system, which was developed by utilizing a custom vehicle detection algorithm and combined with a DeepSORT vehicle tracking algorithm for detecting, tracking, and counting vehicles in highway scenes. It analyzes the performance of the trained vehicle detection model and evaluates the efficiency of the developed vehicle counting method. Furthermore, this section also discusses the vehicle counting experiments that have been conducted by utilizing the edge-computing system platform and live camera inferences obtained by using a Logitech webcam as well as using real-world highway surveillance videos obtained from YouTube. Finally, the results of our vehicle detection model and vehicle counting accuracy scores are presented, discussed, and compared with other similar systems.

3.1 Training Results

The vehicle detection model was trained by utilizing 8,237 images and 2,350 images were used for validation of the model’s performance. The Mean Average Precision, mAP@.5 and the loss function plots were the main metrics used for the evaluation of the trained models. Table 4 presents the model training results obtained after the successful training of four different models. The first model was trained by utilizing the default YOLOv5n model architecture and the original dataset. The second model was trained by utilizing the same default model architecture and by applying data augmentation to the training images. The third model was trained by modifying the YOLOv5n model architecture by adding a small object detection layer and a Convolutional Block Attention Module (CBAM) as well as applying data augmentation to the training images. Finally, the last model was trained by utilizing the same modified YOLOv5n model architecture and the original dataset without applying any augmentations. All of the models were trained for 300 epochs and by utilizing an Nvidia RTX 3060 laptop GPU.

Table 4: Trained Vehicle Detection Models

Data Augmentation	Small Object Detection Layer	CBAM	mAP@.5	Recall	Epochs
			93.2	89.9	300
√			93.6	90.2	300
√	√	√	95.8	92.0	300
	√	√	96.1	91.3	300

The training process for the vehicle detection model requires heavy computation and therefore, we utilized transfer learning techniques and made use of pre-trained weights which have originally been trained on the MS COCO dataset as the starting point for our vehicle detection training process. After the successful training of our highest accuracy model which took 13 hours and 27 minutes to complete, the loss function plots were saved and can be seen in Fig. 8, displaying three main types of losses which are the box, objectness and classification losses. The box regression loss represents how well the algorithm was able to locate the center of the vehicles and how well the predicted bounding boxes covered the detected vehicles. Objectness loss refers to the measure of the probability that a vehicle exists in a predicted region of interest and finally, classification loss refers to the ability of the algorithm to be able to predict the correct vehicle class given a detected vehicle object.

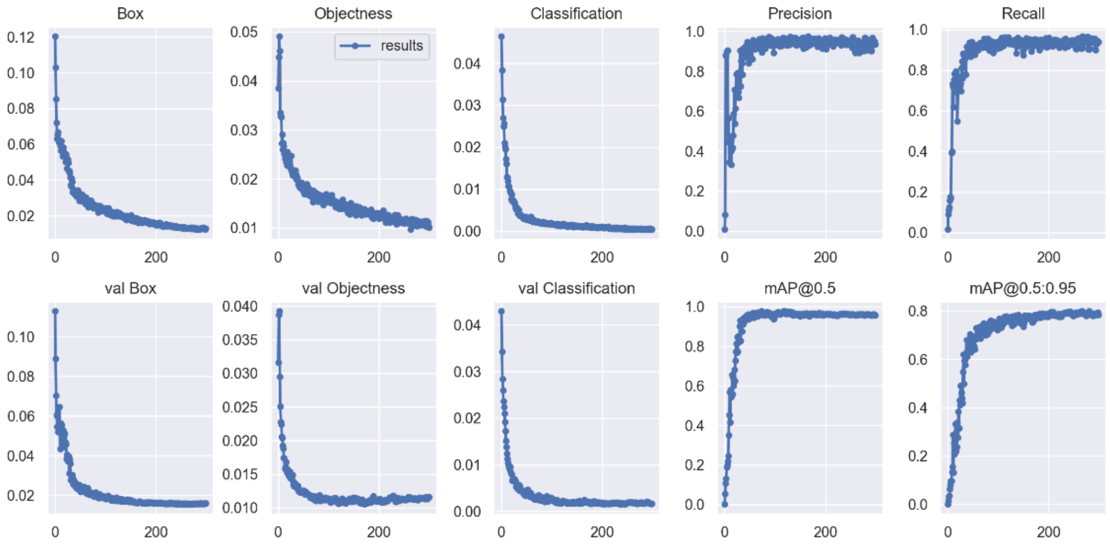

Fig. 8. Model Training Plots over Epochs Results on the Validation set

Precision and Recall are fundamental metrics that are used in object detection to determine whether a trained model is able to make good classifications of detected objects or not. The Precision equation is shown in Eq. (1) and makes use of the True Positive (TP) as well as False Positive (FP) detections in order to determine what proportion of positive vehicle identifications were actually identified correctly. The Recall equation is shown in Eq. (2) and makes use of the True Positive (TP) as well as False Negative (FN) detections to determine what proportion of actual positives were identified correctly. A high Precision and Recall value means that the model is capable of detecting all positive vehicles correctly and that it is able to make accurate classification of the detected vehicles. The Precision-Recall curve for the trained vehicle detection model is shown in Fig. 9.

$$Precision = \frac{True\ Positive}{True\ Positive + False\ Positive} \tag{1}$$

$$Recall = \frac{True\ Positive}{True\ Positive + False\ Negative} \tag{2}$$

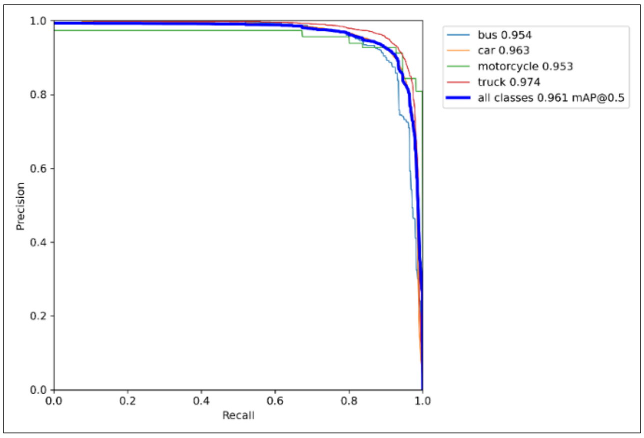

Fig. 9. Precision-Recall Curve

3.2 *Experimental Results*

An edge-computing system platform based on the Nvidia Jetson Nano was integrated and used for testing of our vehicle counting system in real-world test scenarios. The experimental setup was deployed at the Genting Sempah Highway located in Kuala Lumpur, Malaysia and was situated at a pedestrian bridge located approximately 5 meters above the ground. The Logitech C922 Pro HD webcam was pointed directly towards the busy highway and was used for obtaining the live video stream. The Jetson Nano was used for running inference of the trained models and for performing the vehicle detection, tracking, and counting. Finally, the vehicle detection results along with the vehicle counts for each of the vehicle classes, were displayed on a 7-inch LCD display in real-time. Fig. 10 shows the deployed edge-computing system platform used for testing our system.

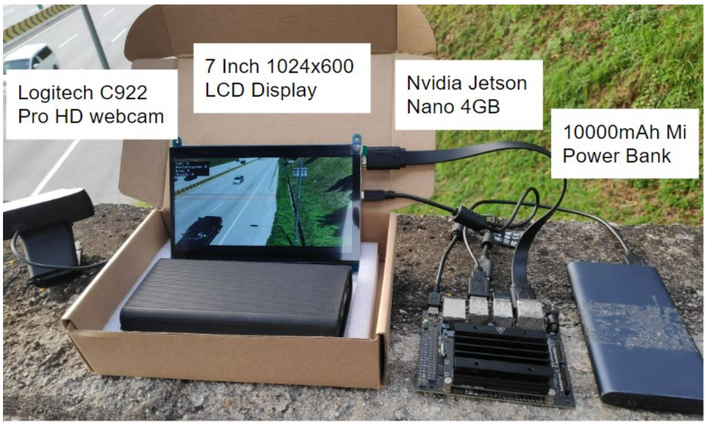

Fig. 10. Edge-computing system platform

Other than the live video inferences, several highway surveillance videos obtained from YouTube were also utilized as input for testing our vehicle counting system. The videos consisted of three one-sided highway videos comprised of various lengths between 0:12 and 01:35 and which are freely available online on YouTube. Table 4.3 summarizes the vehicle counting results obtained for each vehicle class on the video data and the inference results can also be viewed at the following link: https://tinyurl.com/yppcua3d. As can be seen from the inference results, the average speed for running the inference on the 4GB Nvidia Jetson Nano was 15 FPS, close to real-time, and the average vehicle counting accuracy obtained by the system was 95.39%.

3.3 *Discussion*

The loss function plots were found to have converged significantly faster when using the custom model architecture as compared to when using the default YOLOv5n model architecture. At around 200 epochs, the model had already converged with a loss approximately 9.37% lower than that observed when using the default YOLOv5n model architecture. Furthermore, the mean average precision, mAP@.5 is a true measure of the vehicle detection model performance. Fig. 8 shows that after 100 epochs of training, the mAP@.5 of the model gradually stabilizes, reaching approximately 96.02% and after 300 epochs reaching the highest mAP@.5 score which was 96.1%. Data augmentation was applied to the training images, which helped to increase the Recall of the model and the ability to detect most of the positive vehicles correctly; however, the Precision of the model was reduced which resulted in an increase in the number of false positive predictions.

Table 6: Vehicle Counting Performance of our System

Video Name	Duration (minutes)	Vehicle	Counting		Counting Error	Overall Accuracy
			Real	System		
Genting Highway Traffic Cars, Motorcycle, Trucks	01:35	Car Motorcycle Bus Truck	66 1 0 5	64 1 0 2	+2 0 0 +3	93.06%
Live Motorway Traffic in Aceh Indonesia	00:59	Car Motorcycle Bus Truck	24 4 0 1	23 4 0 2	+1 0 0 +1	93.10%
Sample Video Cars Traffic – 27260	00:12	Car Motorcycle Bus Truck	11 0 0 0	11 0 0 0	0 0 0 0	100%
					Average Accuracy	95.39%

The vehicle detection accuracy score was compared with the original YOLOv5n model architecture as the baseline which had achieved an average mAP@.5 score of 93.2% on the same validation set. The model accuracy score was also compared with other similar vehicle detection models such as [1] which made use of the YOLOv3 network and an ORB algorithm for the detection of vehicles in highway scenes and had obtained an average mAP@.5 score of 87.88%. Another method was that developed by [9] which made use of the YOLOv4 network for the detection of vehicles and achieved an average mAP@.5 score of 82.08%. Our proposed algorithm was able to surpass both of these models in terms of the average mAP score, however, because the data used for testing both of the following models have not been open-sourced, accurate comparisons with our proposed model were not possible. Moreover, our vehicle detection accuracy score was averaged on four vehicle classes, meanwhile, most of the other systems developed for the task of vehicle counting are only trained on a single vehicle class.

With regard to vehicle counting, our proposed vehicle counting method was able to achieve an average vehicle counting accuracy score of 95.39%. The vehicle counting accuracy was compared with other methods such as [10] which made use of a virtual distance measurement line counter for counting cars, motorcycles, buses and trucks similar to our system and had achieved an average counting accuracy of 92.20%. Another method was that developed by [1] which made use of a virtual line counter for the counting of cars, buses and trucks and achieved an average vehicle counting accuracy of 93.20%. Furthermore, not only is our proposed system able to obtain higher vehicle counting accuracy results, but it also consists of a lightweight vehicle detection model and a fast ReID model, achieving an average inference speed of 15 FPS on a compact 4GB Nvidia Jetson Nano and 67 FPS on an RTX 3060 laptop GPU.

4. CONCLUSION

In conclusion, our qualitative analysis has proven that our proposed vehicle counting system which was developed by utilizing a custom vehicle detection algorithm based on the YOLOv5n model architecture, combined with a DeepSORT object tracking algorithm and a lightweight OSNet ReID model, is suitable for the task of vehicle detection, tracking and counting in highway scenes. Furthermore, a custom "virtual polygon area" counting approach was also introduced which allowed for accurate and efficient vehicle counting results and avoided duplicate counts. The following system is lightweight and was able to be deployed in real-world scenarios by utilizing an edge-computing system platform based on the Nvidia Jetson Nano. It was able to achieve excellent vehicle detection as well as counting results and is ready to be implemented in real-world applications.

REFERENCES

[1] H. Song and H. Liang, “Vision-based vehicle detection and counting system using deep learning in highway scenes,” vol. 4, 2019.

[2] Z. Luo *et al.*, “Details of the MIO-TCD dataset for vehicle MIO-TCD : A new benchmark classification and localization in press at IEEE Transactions on Image Classification challenge dataset Localization challenge dataset Click here to download the entire dataset :,” pp. 1–9, 2018.

[3] G. Jocher *et al.*, “ultralytics / yolov5 : v6 . 1 - TensorRT , TensorFlow Edge TPU and OpenVINO Export and Inference,” pp. 4–11, 2020.

[4] P. R. Gunjal, B. R. Gunjal, H. A. Shinde, S. M. Vanam, and S. S. Aher, “Moving Object Tracking Using Kalman Filter,” *2018 Int. Conf. Adv. Commun. Comput. Technol. ICACCT 2018*, pp. 544–547, 2018, doi: 10.1109/ICACCT.2018.8529402.

[5] I. C. Vision, “Computer Vision for Multi-Object Tracking — Live Example,” pp. 1–17, 2019.

[6] D.-L. Dinh, H.-N. Nguyen, T. Thai, and K.-H. Le, “Towards AI-Based Traffic Counting System with Edge Computing,” *J. Adv. Transp.*, vol. 2021, pp. 1–15, 2021, doi: 10.1155/2021/5551976.

[7] F. Herzog, X. Ji, T. Teepe, S. Hörmann, J. Gilg, and G. Rigoll, “Lightweight Multi-Branch Network for Person Re-Identification,” *Proc. - Int. Conf. Image Process. ICIP*, vol. 2021-Septe, pp. 1129–1133, 2021, doi: 10.1109/ICIP42928.2021.9506733.

[8] NVidia Corporation, “Jetson NANO Module,” 2019, [Online]. Available: https://developer.nvidia.com/embedded/jetson-nano

[9] M. A. Bin Zuraimi and F. H. Kamaru Zaman, “Vehicle detection and tracking using YOLO and DeepSORT,” *ISCAIE 2021 - IEEE 11th Symp. Comput. Appl. Ind. Electron.*, pp. 23–29, 2021, doi: 10.1109/ISCAIE51753.2021.9431784.

[10] M. Fachrie, “A Simple Vehicle Counting System Using Deep Learning with YOLOv3 Model,” *J. RESTI (Rekayasa Sist. dan Teknol. Informasi)*, vol. 4, no. 3, pp. 462–468, 2020, doi: 10.29207/resti.v4i3.1871.

ASIAN JOURNAL OF ELECTRICAL AND ELECTRONIC ENGINEERING
Vol. 2 No. 2 2022
E-ISSN: 2785-8189

Performance Analysis of a Hybrid Free Space Optics/ Visible Light Communication Systems

Siti Hajar Ab Aziz [1,3]*, Norhanis Aida M. Nor[2], M. Shahnan Zainal Abidin[3]

[1]Communication Technology Section,
Universiti Kuala Lumpur British Malaysian Institute, Kuala Lumpur, Malaysia
[2]Dept. of Science in Engineering, Faculty of Engineering,
International Islamic University Malaysia, Kuala Lumpur, Malaysia
[3]Dept of Electrical and Computer Engineering, Faculty of Engineering,
International Islamic University Malaysia, Kuala Lumpur, Malaysia

*Corresponding author: hajaraziz@unikl.edu.my

(Received: 14th August 2022; Accepted: 26th August 2022)

Abstract— A hybrid free space optical (FSO)/visible light communication (VLC) system is a remarkable wireless technology for overcoming the last mile gap and for future broadband wireless communication. In detail, this research examines the hybrid FSO/VLC system performance using Optisystem 19 software. The system performance of the wireless hybrid FSO/VLC is evaluated using the bit error rate, quality factor, and eye diagram for weak and strong turbulence regimes referring to the Gamma-Gamma atmospheric turbulence channel. At BER of 10^{-9} the maximum attainable distances are 1.3 km and 1.8 km for 0 dBm and 5 dBm transmitted power in clear weather, respectively. However, when the transmit power reduces to -5 dBm, the measured BER drops to 8×10^{-3} with a distance of 1 km link range. Moreover, when the power increases from 0 dBm to 5 dBm, the distance of the connection between Tx and Rx can be extended from 1.1 km and 1.9 km under weak turbulence conditions at the target BER of 10^{-9}. In contrast, at the same target of BER, only 5 dBm of transmitted power managed to capture the signal at a distance of 1.7 km for strong turbulence conditions. This result can be the benchmark research to investigate and identify the best strategies for validating future experimentation difficulties.

Keywords: *Free space optics (FSO), Visible light communications (VLC), Atmospheric turbulence, and Hybrid FSO/VLC.*

1. INTRODUCTION

The growth of wireless devices and technologies is swift and dynamic due to the high demand for reliable, seamless, and high-speed connectivity. Cisco Annual Internet Report forecasted in [1] that the world will have 5.3 billion cybercitizens, 14.7 billion machine-to-machine (M2M) applications, 29.3 billion networked devices, and 628 million public Wi-Fi hotspots in 2023. This increment is due to greater access to smart devices such as smartphones and deployed wearable devices. Most of the available wireless technologies/devices, such as Wi-Fi, cellular and Bluetooth, are based on radio frequency (RF) transmission technology, which cannot satisfy the demand for data transfer, backhaul issues and transmission interruption [2]. This will lead to fine-grained traffic and spectrum crunch, specifically at the "last-mile" and "last meter" access linkages. Even though there are various advancements in RF technology, the accessible RF spectrum is significantly congested [3]. Optical wireless communication (OWC) is one possible solution, complementary to RF wireless systems, which enables the fastest and most reliable data exchange in specific applications indoors and outdoors, mainly to alleviate the pressure on the RF spectrum crisis. The applications include very short-range (mm range), outdoor intra-building linkages (a few km range), and inter-satellite communication (4500 km range). OWC are classified into three main categories based on their operating wavelength: ultraviolet light (100 nm – 400 nm), visible light (380 nm – 780 nm), and infrared light (IR) (800 nm – 2500 nm) [2].

Well known as one of the matured OWC technology, the free space optics (FSO) communications system is commonly utilized for outdoor communications links. It has frequently been employed in various applications, including the resolution of the last-mile bottleneck issue, backhaul for cellular systems, inter-building connections, broadband access in remote locations, and wireless metropolitan area network extensions [3], [4]. This is because of the unique features offered by FSO systems, which include a high data rate with almost unlimited bandwidth, a superior level of security against eavesdropping, low cost of deployment, and resilience to RF-induced electromagnetic interference. Regardless of the benefits, the FSO link is impacted by atmospheric phenomena, including snow, fog, smog, rain and turbulence. In clear weather, air turbulence becomes the main challenge as it generates random variations in the phase and intensity of the light signal, which ultimately results in system performance degradation [5], [6]. There are various number of mitigation schemes to mitigate the impact of atmospheric conditions, including*(i)* coding; *(ii)* aperture averaging; *(iii)* relay-assisted; *(iv)* complex modulation; *(v)* diversity; and *(vi)* adaptive threshold detection [3], [7].

Therefore, this research investigates the performance of hybrid FSO/VLC systems for interconnection between outdoor and indoor environments under weak and strong turbulence conditions using the Optisystem 19 software. The maximum distance under turbulence conditions is investigated based on the transmitted optical power of 0 dBm and 5 dBm. Then, the system's performance is analyzed and evaluated in weak and strong turbulence conditions as specified by the Q-factor, bit error rate (BER), and eye diagrams.

The remainder of this paper is presented as follows: Section 2 explains a hybrid FSO/VLC system under turbulence conditions. The findings are presented concisely in Section 3, along with the effects of various laser optical power approaches. Lastly, the conclusion is presented in Section 4.

2. THE HYBRID FSO/VLC LINK

2.1 *Overview of the hybrid FSO/VLC system*

The benefits of OWC, mainly FSO and VLC technologies, enable the possibility of merging them into a hybrid optical wireless network [8]. The optical-optical wireless hybrid approach is a feasible alternative for enhancing seamless connectivity and fulfilling user quality of service (QoS) requirements for high wireless data rates. The authors [3], [10], [12] claimed that both FSO and VLC technologies are strong enough to endure bandwidth bottleneck issues in the interconnection of outdoor to indoor networks, particularly in highly dense urban areas with a high number of access points. The first demonstration of the hybrid FSO/VLC was done by [13], specifically for tomorrow's indoor wireless broadband access by integrating the outside FSO and the inside VLC system through a single-mode fibre (SMF). The author achieved bit rates up to 300 Mbit/s utilizing 16- quadrature amplitude modulation (QAM) or 32 -QAM- single carrier with frequency domain equalization (QAM-SC-FDE) modulation [13]. Next, a hybrid FSO/VLC heterogeneous interconnection was demonstrated to overcome the wireless network reliability issue and electromagnetic interference levels in a hybrid RF/FSO system [3], [8]. Recently, a lower-cost and portable hybrid RF/VLC/FSO system for indoor communication was demonstrated in [10]. The results showed a data rate of 1 kbps at a 4 cm transmission link. They suggested FSO as a backbone network solution in the last mile access linkage located at the various lighting points in multiple users' enclosed rooms within a building.

To the best author's knowledge, there is still a lack of investigation on FSO/VLC hybrid systems in the literature, with just five experimentally based publications. In addition, the system's performances under turbulence conditions have not been investigated using any simulation tool. This work is a preliminary study investigating and identifying the best strategies for validating future experimentation difficulties.

2.2 *Atmospheric Turbulence Influence*

Atmospheric turbulence is a random occurrence resulting from atmospheric variations in pressure and temperature, which produce variations in the atmosphere's refractive index and transmission medium [5]. Due to the redistribution of signal energy, this occurrence will lead to fluctuations in the received signal's strength and phase. This inhomogeneity of the two factors creates a turbulent cell that either constructively or destructively interferes with the propagating beam. The parameter $C_n^2$of the refractive index structure measures the turbulence intensity and is acquired from [5], [7], [14]:

$$C_n^2 = (86 \times 10^{-16} \times \frac{P}{T^2})^2 C_T^2 \ , \tag{1}$$

where C_T^2 denotes the temperature structure constant based on the general 2/3 power temperature law, and P denotes the atmospheric pressure in millibar. T denotes the absolute temperature in Kelvin. Furthermore, the Rytov variance, $\boldsymbol{\sigma_R^2}$ characterizes the turbulence regime, which is derived from [5], [7], [14].

$$\sigma_R^2 = 1.23\ C_n^2 k^{\frac{7}{6}} L^{\frac{11}{6}}, \tag{2}$$

where L denotes the propagation path length, and k represents the optical wave. Derived from (2), C_n^2 computes the refractive index fluctuation of strong turbulence (10^{-12} $m^{-2/3}$) and weak turbulence(10^{-16} $m^{-2/3}$).

2.3 *Simulation Design and Setup Analysis*

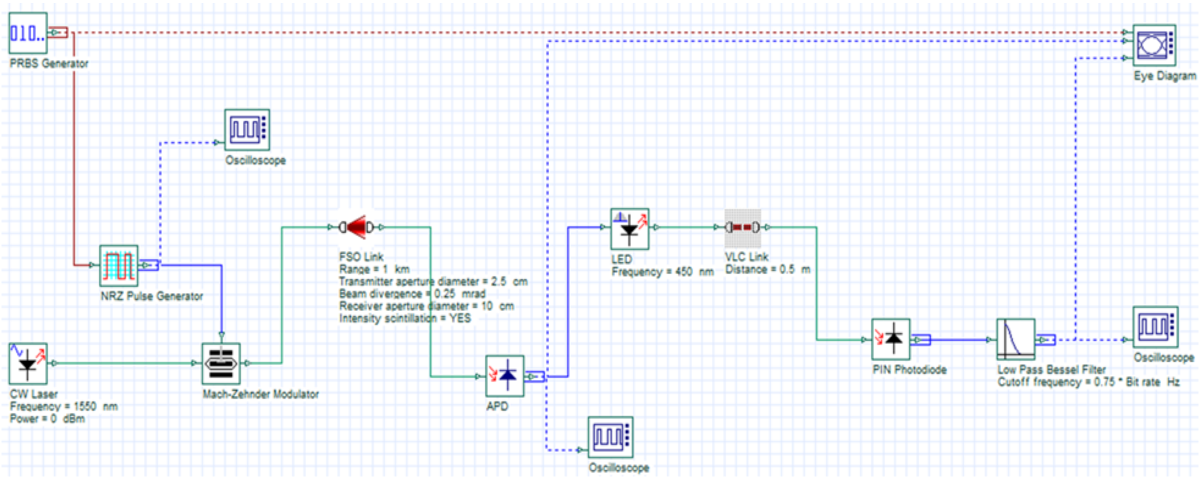

Fig. 1. The hybrid FSO/VLC link

The proposed hybrid FSO/VLC system is illustrated in Fig. 1. The links consist of 2 sections: the FSO link and the VLC link, which are interconnected with SMF fibre. At the transmitter (Tx) side, a BER tester with a 1 Gbps data rate was modulated using the non-return-to-zero on-off keying (NRZ-OOK) format to generate the electrical signal. The electrical signal and the optical source were modulated in the Mach-Zehnder (MZ) modulator, functioning 1550 nm with 0 dBm output power. Then, the modulated optical input signal is transmitted to the FSO channel of the linkspan of 1 km.

At the FSO channel, the optical Tx and receiver (Rx) aperture diameters were set to 2.5 cm and 10.0 cm, respectively. The beam divergence value was 0.25 mrad, consistent with most FSO commercial systems. Next, an avalanche photodiode (APD) was used at the Rx to detect and demodulate the light signal before being coupled with the direct current (DC) signal and applied to the white LED.

The Tx and Rx of the VLC system are in a line of sight (LOS) condition to optimize the light signal quality without considering the reflected light or ambient light from surrounding walls. At the VLC link, a single LED was considered the Tx, operated at the peak wavelength of 450 nm and biased at ~350 mA following the commercial parameters [15]. The gap between the LED and the detector was 0.5 m. The silicon biased detector ranging from 350 to 1100 nm was used for signal detection and demodulation before it was passed to the low-pass Bessel filter with a 0.75 GHz cut-off frequency for signal filtering.

Lastly, the demodulated signal was passed to the eye diagram analyzer for system investigation and evaluation. In order to investigate the robustness of the proposed system over turbulence, the turbulence regime was considered at the FSO channel, classified as a weak condition ($C_n^2 = 5 \times 10^{-15} m^{-2/3}$) and a strong condition ($C_n^2 = 5 \times 10^{-12}\ m^{-2/3}$). The hybrid FSO/VLC link system was constructed according to the link parameters of a typically practical and commercial FSO system, depicted in Table 1.

Table 1: The hybrid FSO/VLC system parameters

Parameters	*Value*
Data rate	*1 Gbps*
Continuous Wave (CW) Laser	
Operating wavelength	*1550nm*
Power	*0 dBm*
FSO Link	
Range	*1km*
Transmitter aperture diameter	*2.5cm*
Beam divergence angle	*0.25mrad*
Receiver aperture diameter	*10cm*
APD photodiode	
Gain	*3*
Responsivity	*1A/W*
Dark current	*10 nA*
LED	
Wavelength	*450nm*
Electron lifetime	*1 ps*
RC constant	*1 ps*
VLC	
Distance	*0.5m*
Transmitter half (1/2)-angle	*60°*
Irradiance half (1/2)-angle	*20°*
Incidence half (1/2-angle	*20°*
PIN photodiode	
Responsivity	*1A/W*
Dark current	*10nA*

3. RESULTS AND DISCUSSIONS

The hybrid FSO/VLC system is evaluated using the quality metric (*Q*-factor), BER and eye diagram. Typically, it is used to evaluate the performance of optical fibre communication (OFC) and optical wireless communication (OWC), also related to the electrical signal-to-noise ratio (SNR) and BER. Additionally, Q-factor represents the SNR for digital optical communication. Remarkably, the greater the *Q*-factor, the better the quality of the signal. The *Q*-factor from BER is based on [16]:

$$BER = \frac{1}{2} erfc\left(\frac{Q}{\sqrt{2}}\right), \tag{3}$$

where *erfc* represents the complementary error function, the *Q*-factor is calculated by [4] :

$$Q = \frac{V_H - V_L}{\sigma_H - \sigma_L}, \tag{4}$$

where V_L and V_H represent the mean value of the low and high voltages received, σ_H represents high standard deviation and σ_L is a low standard deviation.

The eye diagrams and *Q* - factors at the aforementioned values of no turbulence, weak turbulence and strong turbulence are depicted in Fig. 2. Typically, the quality of the hybrid system deteriorates according to the turbulence strength. Under a clear atmospheric condition, the *Q*-factors are 2.41, 7.17 and 13.29 for -5 dBm, 0 dBm and 5 dBm transmitted power. We introduced the turbulence to the FSO channel with the same range of transmitted power. For $C_n^2 = 5 \times 10^{-15} m^{-2/3}$(weak turbulence), the *Q*-factors are 3.0, 6.92, and 12.76 for transmitting power of -5 dBm, 0 dBm, and 5 dBm, correspondingly. Concurrently, the eye-opening and *Q*-factor significantly degraded as the C_n^2 increases to $5.0 \times 10^{-12} m^{-2/3}$, which is classified under strong turbulence. The figure shows that the eye diagram is completely shut at -5 dBm transmit power. In order to capture the signal, the transmit power should be increased to at least 0 dBm with a *Q*-factor of 3.28. Moreover, the *Q*-factor and eye-opening will be much better as the transmit power increases. These results show that the propagating optical wave suffers more intensity variations at higher degrees of turbulence resulting in a significantly broader and random optical beam pattern at higher intensity levels[17]. Based on the results, signal distortion increases as the Q-factor decreases, resulting in a narrower eye-opening.

-5 dBm	0 dBm	5 dBm
No Turbulence		
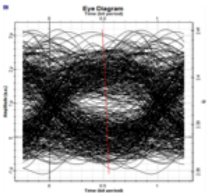 Q-factor = 2.41	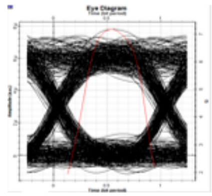 Q-factor = 7.17	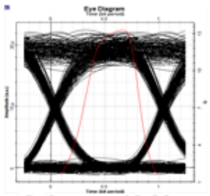 Q-factor = 13.29
$C_n^2=5.0\times10^{-15}\ \mathrm{m}^{\frac{-2}{3}}$		
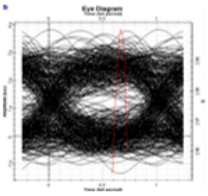 Q-factor = 3.00	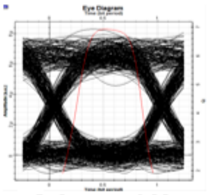 Q-factor = 6.92	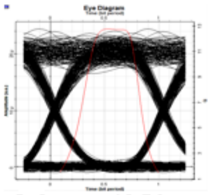 Q-factor = 12.76
$C_n^2=5.0\times10^{-12}\ \mathrm{m}^{\frac{-2}{3}}$		
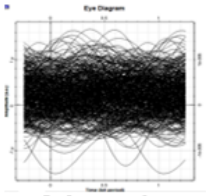 Q-factor = 0	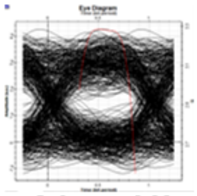 Q-factor = 3.28	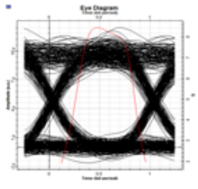 Q-factor = 8.50

Fig. 2. Eye diagrams and the *Q*- factor at different atmospheric conditions

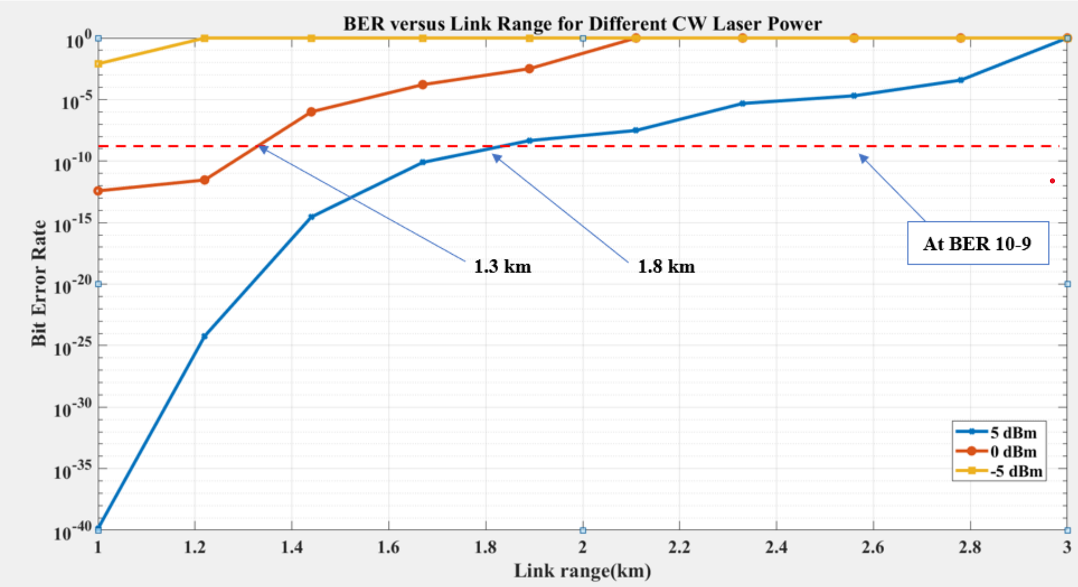

Fig. 3. The BER performance in a clear atmosphere

Then, we analyzed the result of transmitting optical power over the link distance. Fig. 3 compares the transmitted optical power for BER performance against the link distance, ranging from 1 km to 3 km in a clear atmosphere. The minimum required BER for telecommunication applications is 10^{-9}. As shown in Fig. 3, at a BER of 10^{-9}, the signal can be transmitted up to distances of 1.3 km and 1.8 km for 0 dBm and 5 dBm transmitted power, respectively. Despite, when we used -5 dBm transmitted power, no signal was detected at the Rx when the link range was more significant than 1 km. For 5 dBm transmit power, the links can be extended up to 2.8 km with a BER of ~10^{-3}. This result proves that the BER performance increases as the transmitted power increases, which yields to increases in the linkspan.

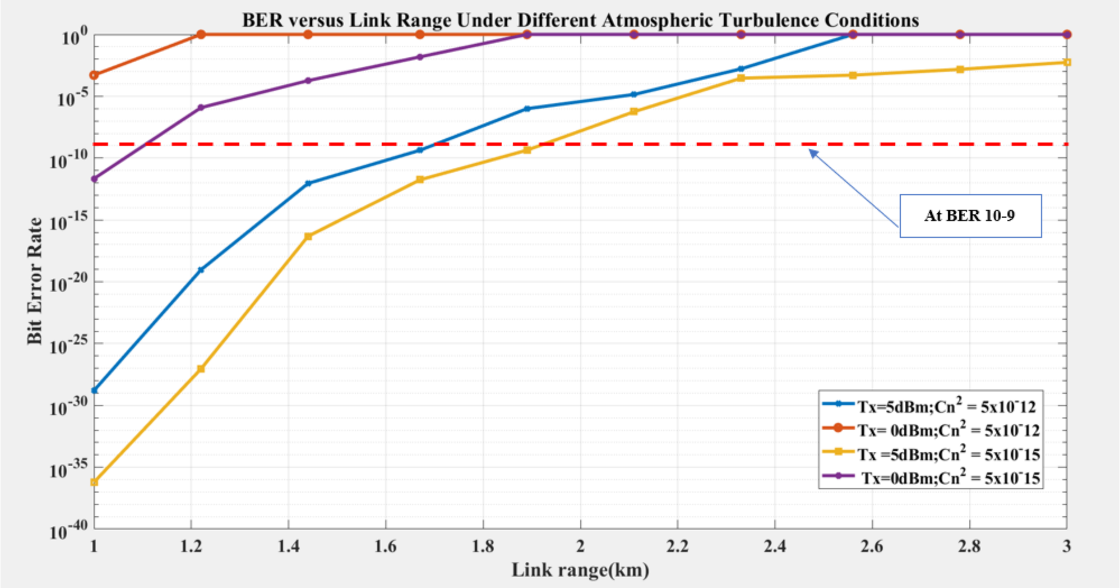

Fig. 4. The BER under turbulence influences

Next, we analyzed the system performance under weak and strong turbulence for 0 dBm and 5 dBm transmitted power to examine the maximum achievable distances at the FSO link. Fig. 4 shows the effect of BER against the link range under weak $(C_n^2 = 5 \times 10^{-15} m^{-2/3})$ and strong $(C_n^2 = 5 \times 10^{-12} m^{-\frac{2}{3}})$ turbulence regimes. Theoretically, the link range between the Tx and the Rx will be lengthened as the power increases. In Fig. 4, we prove that as the power increases from 0 dBm to 5 dBm, the distance increases from 1.1 km to ~1.9 km at BER of 10^{-9} in weak turbulence form. Under strong turbulence, at BER of 10^{-9}, the signal can only be captured when the transmit power is 5 dBm, with the link distance is 1.7 km. As illustrated in the figure, only the FSO link under weak turbulence with 5 dBm power managed to obtain 3 km linkspan with BER of 10^{-3}. It can be concluded that by increasing the transmitted optical power, there is an improvement in the BER result and link distance for all weather conditions, thus enhancing overall system performance. However, the penalty increases in cost as the power increases. In addition, the average BER decreases as the scintillation index increases. Hence, a mitigation strategy is vital to increase the transmission range.

4. CONCLUSION

This work presented a performance analysis of hybrid optical wireless systems, particularly FSO/ VLC systems, in the presence of atmospheric turbulences. The impact of transmitted optical power in clear atmospheric, weak, and strong turbulence conditions was carried out to assess the hybrid system's performance. The performance was quantified using the Q-factor, BER and eye diagram. In clear weather, the achievable distances were 1.3 km and 1.8 km for 0 dBm and 5 dBm transmitted optical power at a BER of 10 -9. However, with -5 dBm transmitted power, the BER was reduced to 8×10 -3 for a 1 km range. Moreover, when Tx transmits 5 dBm power, the BER is 10^{-37} for weak turbulence and $10^{-29}$for strong turbulence in 1 km range. At 3 km, only the FSO link under weak turbulence with 5 dBm power was managed to obtain the result. Therefore, we need to address an effective technique to enhance the hybrid FSO/VLC systems, considering both FSO and VLC links limitations.

ACKNOWLEDGMENT

This work has been sponsored by the Ministry of Higher Education Malaysia (MOHE) under the Fundamental Research Grant Scheme (FRGS) RACER/1/2019/TK04/UIAM//3 and Universiti Kuala Lumpur British Malaysian Institute.

REFERENCES

[1] Cisco, "Cisco: 2020 Annual Internet Report," Computer Fraud & Security, 2020.

[2] M. Z. Chowdhury, M. K. Hasan, M. Shahjalal, M. T. Hossan, and Y. M. Jang, "Optical Wireless Hybrid Networks: Trends, Opportunities, Challenges, and Research Directions," IEEE Communications Surveys and Tutorials, pp. 930–966, Apr. 2020.

[3] P. Pesek, S. Zvanovec, P. Chvojka, Z. Ghassemlooy, and P. A. Haigh, "Demonstration of a hybrid FSO/VLC link for the last mile and last meter networks," IEEE Photonics Journal, 2019.

[4] N. A. and S. Siti Hajar Ab Aziz, "Performance Analysis of Free Space Optics Link Under the Effect of Rain Attenuation," 2021.

[5] L. Cang, H. K. Zhao, and G. X. Zheng, "The Impact of Atmospheric Turbulence on Terahertz Communication," IEEE Access, vol. 7, pp. 88685–88692, 2019.

[6] N. A. M. Nor, et al., "Experimental all-optical relay-assisted FSO link with regeneration and forward scheme for ultra-short pulse transmission," Optics Express,p. 22127, 2019.

[7] N. A. M. Nor et al., "Experimental investigation of all-optical relay-assisted 10Gb/s FSO link over the atmospheric turbulence channel," Journal of Lightwave Technology, pp. 45–53, Jan. 2017.

[8] Z. Huang et al., "Hybrid optical wireless network for future SAGO-integrated communication based on FSO/VLC heterogeneous interconnection," IEEE Photonics Journal, pp. 1–10, 2017.

[9] X. Li, Z. Ghassemlooy, S. Zvanovec, R. Perez-Jimenez, and P. A. Haigh, "Should Analogue Pre-Equalizers be Avoided in VLC Systems?," IEEE Photonics Journal, pp. 1–14, 2020.

[10] I. E. Lee et al., "Design of a hybrid free space optical and visible light communication system for indoor wireless data broadcasting," Journal of Physics: Conference Series, vol. 1432, no. 1, 2020.

[11] S. R. Teli, S. Zvanovec, and Z. Ghassemlooy, "Optical internet of things within 5g: Applications and challenges," Proceedings - 2018 IEEE International Conference on Internet of Things and Intelligence System, IOTAIS 2018, pp. 40–45, 2019.

[12] B. G. Guzman et al., "Reflection-based relaying techniques in visible light communications: Will it work?," IEEE Access, pp. 80922–80935, 2020.

[13] Z. Zheng, L. Liu, T. Chen, and W. Hu, "Integrated system of free-space optical and visible light communication for indoor wireless broadband access," Electronics Letters, pp. 1943–1944, 2015.

[14] N. S. Sadzali, N. A. M. Nor, and S. H. B. A. Aziz, "Performance Analysis of FSO Systems using Different Modulation Techniques under the Influence of Atmospheric Turbulence," pp. 397–400, 2021.

[15] O. O. Semiconductors, "Golden DRAGON Datasheet Version," pp. 1–21, 2016.

[16] S. Burdah et al., "Performance analysis of Q factor optical communication in free space optics and single mode fiber," Universal Journal of Electrical and Electronic Engineering, pp. 167–175, 2019.

[17] N. A. M. Nor et al., "10 Gbps all-optical relay-assisted FSO system over a turbulence channel," 2015 4th International Workshop on Optical Wireless Communications, IWOW 2015, no. September, pp. 69–72, 2015.

ASIAN JOURNAL OF ELECTRICAL AND ELECTRONIC ENGINEERING
Vol. 2 No. 2 2022
E-ISSN: 2785-8189

Analysis and Optimization of Fuzzy Logic Based MPPT for Grid Connected Photovoltaic System

Ahmad Mmzr Alazmi, S M Salam*, Muhammad Mahbubur Rashid

Department of Mechatronics, Faculty of Engineering,
International Islamic University Malaysia
Kuala Lumpur, Malaysia

*Corresponding author: sm.salam@ustc.ac.bd

(Received: 31st August 2022; Accepted: 13th September 2022)

Abstract— Solar is one of the most important renewable energy sources that consistently operates with clean, sustainable, and ecologically beneficial operations in the photovoltaic power producing station. Additionally, due to the nature of photovoltaic power, the fluctuating trend in PV system output energy reduces their dependability in terms of supplying consumers with uninterrupted energy. A significant benefit of photovoltaic (PV) structures is their capacity to harness the immense and unpredictable power of the sun. Strong sunlight environments have accelerated PV science, which is now present in high-efficiency regions and regions with frequent cloud cover. A modeling approach for renewable grid-connected microgrids is presented in this research. Under gloomy or foggy situations, the long rambling factor makes up the majority of solar insolation. This work simulates a PV system using MATLAB and uses a fuzzy method to monitor the component that consumes the most energy. The findings of the fuzzy Logic version were improved for validation, and they were also contrasted with those from other methods like perturb and observe (P&O) and proportional integral differential (PID).

Keywords: *PV, Grid connected PV, Fuzzy logic based MPPT, MATLAB simulation and Optimization.*

1. INTRODUCTION

After the energy crisis and environmental problems, including pollution and global warming, solar photovoltaic (PV) systems have attracted a lot of research attention. Regarding the effectiveness of solar photovoltaic systems, additional research is now being done on how to extract more electricity efficiently from PV cells. The output voltage of solar PV systems varies with sun irradiation and temperature variations, which is their primary flaw. One maximum power point (MPP) from the photovoltaic array input is tracked by the Maximum Power Point Tracking (MPPT) procedure. Automatically determining the voltage MPPT or current MPPT at which a PV array should run to attain the MPPT maximum output at the specified temperature and irradiance. It is noticed that the P-V characteristics of the PV array become more complicated and exhibit several peaks under partial shade situations [1]. Several MPPT tracking strategies are in use, and comparisons between the majority of these MPPT approaches and the quantity of energy harvested from the PV panel have been made in the literature [2–3]. Perturb and Observe (P&O) and the Incremental Conductance (IC) algorithm are the two most often used MPPT algorithms.

Different MPPT types have been created and introduced [4-5]. Fuzzy logic is an excellent approach for determining a solar panel's MPP and has strong stability and a high reaction rate. Since it has superior performance, accuracy, and stability, fuzzy-based MPPT [6-7] research papers have been published more recently. To improve the effectiveness and reliability of solar photovoltaic (PV) power generation, the author [8–9] suggests a fuzzy-based MPPT and constructs a dynamic model of a grid-connected PV system using the MATLAB/Simulink environment. The system with fuzzy-based MPPT boosts energy production efficiency, according to simulation data. A novel fuzzy-based method was suggested in Reference [10] and compared to the others to track the solar panel's most significant power.

Photovoltaic systems require installing power conversion equipment between the PV array and the Grid. With steady-state operation on the grid side, the control is intended to produce PV software quality with MPPT algorithm performance and high load current harmonics for generator PV applications. The PV array should operate over the estimated voltage and current at maximum power output in order to generate the most electricity, independent of the weather. The MPPT system does this. The power converter converts the PV array's DC to an electrical current. A DC-AC converter converts DC to AC with a unity power factor for grid-connected applications.

In contrast, a DC-DC converter often performs MPP and voltage boosting in a two-stage paradigm. A DC-AC converter is used in a single-stage structure to monitor the MPP, regulate the active and reactive power transferred to the Grid, and change the DC produced by the PV array into AC. The high-frequency components of the AC inverter current are filtered via the grid interface to deliver low total harmonic distortion AC to the Grid. For grid-connected PV systems, conventional linear control methods such as proportional-integral (PI), proportional resonant (PR), hysteresis, and predictive controllers have been made accessible by [11] and [12]. The control system performs two kinds of tasks: stabilization and tracking [13]. In a stabilization challenge, the control system's goal is to maintain the closed-loop system's state stable around its equilibrium point.

2. MODELING OF A GRID CONNECTED SOLAR SYSTEM WITH FUZZY LOGIC

Photovoltaic systems require installing power conversion equipment between the PV array and the Grid. These systems are built to function alongside both the Grid and other systems. An MPPT algorithm, an energy exchanger, a meter connection, and a management system make up energy endurance. With steady-state operation on the grid side and high load current harmonics for generator PV applications, the control is intended to produce good PV software quality [14]. The PV array should operate over the estimated voltage and current at maximum power output to generate the most electricity, independent of the weather. The MPPT system does this. The PV array's DC is converted via the power converter.

A DC-AC converter transforms DC to AC with a unity power factor for grid-connected systems, whereas a DC-DC converter often conducts MPP and voltage boosting in the two-stage idea. In a single-stage construction, a DC-AC converter controls the active and reactive power transmitted to the Grid, monitors the MPP, and converts the DC current generated by the PV array to AC current. In order to supply the Grid with AC with low total harmonic distortion, the high-frequency components of the AC inverter current are filtered via the grid interface. [15] and [13] have presented conventional linear control techniques for grid-connected PV systems, including PI controller, Proportional Resonant (PR) controller, and Hysteresis controller.

2.1 *PV systems design*

The data sheet supplied by the manufacturer is frequently the foundation for calculations that replicate the PV parameters. The I-V characteristics are most accurately predicted at a specific operating temperature and sun irradiation. Theoretical models are used to forecast how the PV cell will behave in terms of open circuit voltage, short circuit current, and MPPT algorithm voltage and current. The single diode model (SDM), the most used approximation model, is shown in Figure 1. This model successfully balances simplicity and accuracy (Chen, 2010). The SDM is depicted in a simplified manner in the ideal single diode model (ISDM). Series and shunt resistances are not taken into consideration by the ISDM in figure 1.

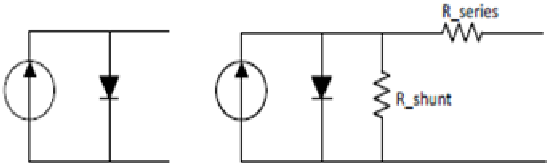

Figure 1: PV representation model

The ISDM model assumes Iph and Id. This thesis uses the SDM model, which is commonly used, simple, and accurate. The efficiency of the PV cell may be increased by first determining the (MPP). When the power change over the voltage changes equals zero, the MPP is attained. We must use one of the Maximum Power

Point Tracking (MPPT) techniques to obtain the MPP. The most popular and often employed methods are "Hill Climbing" methods. The P&O and Incremental Conductance techniques are the two most used for ascending hills. Temperature and solar radiation are two elements that influence the amount of energy that current PV cells generate (temperature).

2.2 Maximum power point technology

A specific strategy was required to find significant solar power with stationary solar panels. To maximize the power point, various techniques have been developed, including, Voltage feedback, Perturbation and Observe (P&O), Incremental Conductance (IncCond), Power feedback, Parabola Prediction, Particle Swarm Optimization (PSO), Fuzzy Logic Control (FLC), Score Open Circuit Voltage, Neural Network (NN), Current Scanning and Adaptive Neuro-Fuzzy Inference System (ANFIS). In the next section, we'll discuss fuzzy logic technology and how it may help you get the highest MPPT output. The MPPT Fuzzy Controller (FLC) (PWM control) is a technique for managing a DC-to-DC converter's electrical output. To lessen the unpredictable nature of PV production, FLC was used.

2.2.1. Fuzzy logic controller design parameters

An example of a fuzzy logic-based maximum power point tracker is shown in Figure 2. The PV module's output voltage and output current (Vm) are the only two state variables the fuzzy controller interprets as inputs, as shown from the observation (Im). The fuzzy logic controller creates a signal proportionate to the converter duty cycle based on measurements and sends it to the converter via a pulse width modulator (D). Pulse width modulation (PWM), which is performed by this modulator, produces the control signals for the converter switch (s). It is known as a closed loop system when referring to fuzzy logic controller technology.

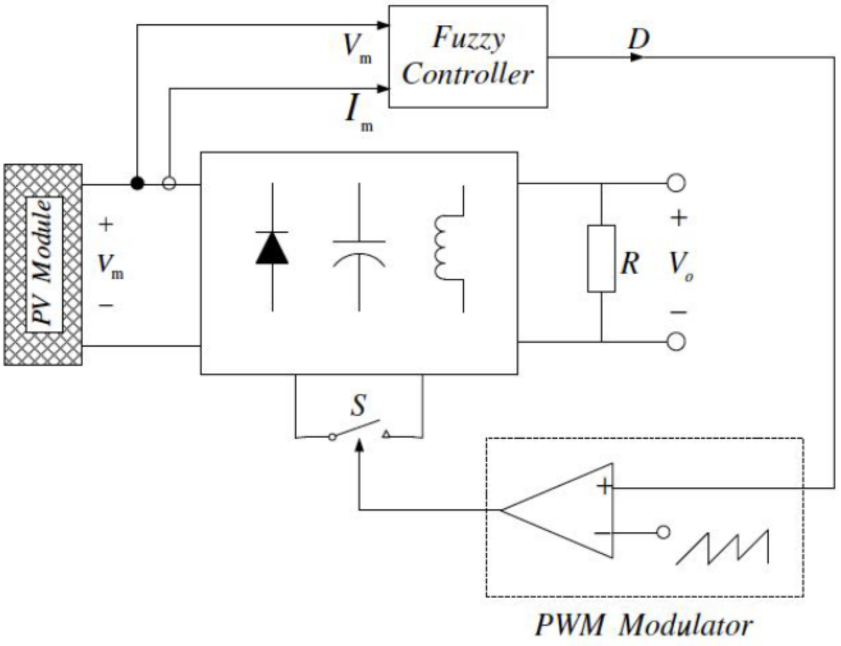

Figure 2: Schematic diagram of Fuzzy Logic Controller

When the fuzzy controller was modified in MATLAB, the FIS file was created so that it could be called in the Simulink system. Figure 3 displays the fuzzy controller's performance after looking at the output at various input values.

The many input and output readings that were taken are listed in Table1. Finally, this reading is used to optimize the fuzzy logic controller's duty cycle. The system was built using Simulink/MATLAB and tested for a variety of solar irradiation levels. The different irradiance fluctuations were simulated using the Simulink/MATLAB simulation model.

Table 5.1: Duty Cycle Optimization table for different values

Current	Voltage	Duty cycle
0.49	11	0.929
0.299	15	0.9169
5	17	0.7293
9.8	18	0.8354
9.9	25.01	0.6102
14.9	17.33	0.6229
15	17.3	0.6429

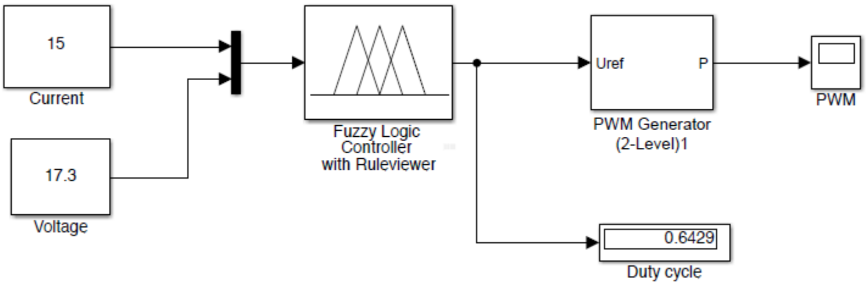

Figure 3: Optimum duty cycle controller in MATLAB

In order to verify the functionality of the fuzzy controller and the effectiveness of the converter, readings of the input power and output power of the MPPT were collected at solar irradiation (1000w/m2, 800w/m2, 600w/m2, 400w/m2, and more) and duty cycle were noted at the same radiation levels. Details regarding the simulation findings are provided in Table 2.

Table 5.2: FLC Simulation results

Irradiance value (W/m^2)	**Power Input in watt**	**Power Output in Watt**	**Value of Duty Cycle**	**Efficiency**
1000	251.7	253	0.65	0.99486166
850	219.7	221.9	0.65	0.99008562
700	170.9	172.7	0.59	0.9895773
550	118.98	120.5	0.49	0.98738589
400	78.86	79.4	0.35	0.99319899

2.3 Fuzzy based MPPT for Grid connected PV system

The Simple P&O technique creates and manages the fuzzy logic based MPPT Controller in uncertain situations. The building block indicates the device's uncertain condition for SIMULINK/signal in MATLAB. The evaluation is completed by comparing the data to determine the most precise and effective method for tracking maximum power in ambiguous situations. The MATLAB/SIMULINK program was utilized to build the model. The output of the PV Module is coupled to the DC-DC Buck-Boost converter, which houses the electric drive.

Fuzzy Logic Based MPPT Controller sends a gate signal pulse to the MOSFET. The controller is designed to keep track of the PV module's maximum power under rapidly changing circumstances. Unpredictable circumstances might be caused by temperature and irradiation level variations. Uncertainty is accepted by the PV Module using a signal block made up of many input signals. In order to make a more realistic comparison, the uncertainty for both strategies is equal. The fuzzy logic controller and MPPT algorithm are connected in this arrangement. The MPPT file, which contains the rules and membership functions for maximizing the output voltage from the solar PV module, is stored by the fuzzy logic controller. The output of the fuzzy logic controller is supplied to the output block, which modulates the signal with the suitable repeated sequencing signal. The input signal block sends the voltage and power change signal to the fuzzy logic controller. The gate drive, a buck-boost converter, receives the output after that. The membership function and rule evaluations define the output of the fuzzy logic controller. The fuzzy logic controller (FLC) can handle inhomogeneity, functions with assumed inputs, and is not dependent on a precise mathematical model.

Additionally, fuzzy is a lot stronger than a typical non-linear FLC system controller. The four major elements are the inference counting approach, system defuzzification, basis on the rule, and fuzzification [10]. E is the error, and alteration in error, namely CE, at the duty cycle denoted as D, where symbol V(t) along with P(t) is denoted as voltage as well as the power of a PV cell, respectively, are FLC's inputs in this study.

The following are the implied steps:

If dP/dV is greater than 0, the system controller modifies the system's duty cycle to change voltage rises until power is adjusted to the highest value.

If dP/dV is equal to 0, the controller remains with the same duty cycle, the power reaches the highest value

If dP/dV is smaller than 0, the change in the controller duty cycle is maintained the voltage value decreases until power is adjusted to the highest value.

Based on five fuzzy sets, negative small (NS), negative large (NB), positive small (PS), positive big (PB), and zero, membership function values are assigned to the linguistic variables (ZE). Figure 4 shows how fuzzy subsets are divided and how membership functions may take different forms depending on duty cycle implemented at the system, as demonstrated in Figures 5 to 6. The uncertainty for both strategies should be identical to allow for a more accurate comparison. The fuzzy logic controller and the MPPT algorithm are connected in this architecture. The MPPT file is kept in the fuzzy logic controller and contains the rules and membership functions for getting the most significant output voltage from the solar PV module.

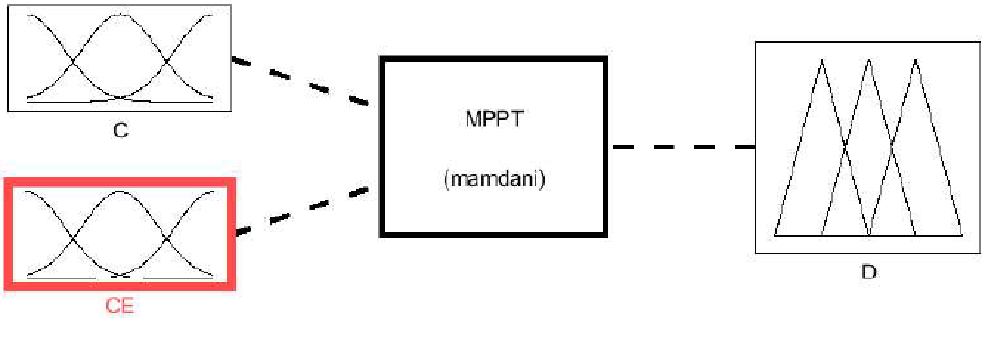

Figure 4: Fuzzy controller Model

For a more accurate comparison, the uncertainty for both techniques is equal. The fuzzy logic controller is linked to the MPPT algorithm in this architecture. The MPPT file, which contains the rules and membership functions for achieving the highest output voltage from the solar PV module, is stored in the fuzzy logic controller.

The fuzzy logic controller receives a voltage and power change signal from the input signal block, and the output of the fuzzy logic controller is supplied to the output block, which modulates the signal with the suitable repeated sequencing signal. The buck-boost converter's final output is then sent into the gate of an IGBT. The membership function and rule evaluations are used to determine the fuzzy logic controller's output.

At first, we use three membership functions to optimize the fuzzy logic controller and the output is stored in the table. For the next step, we use another fuzzy logic system table with five membership functions.

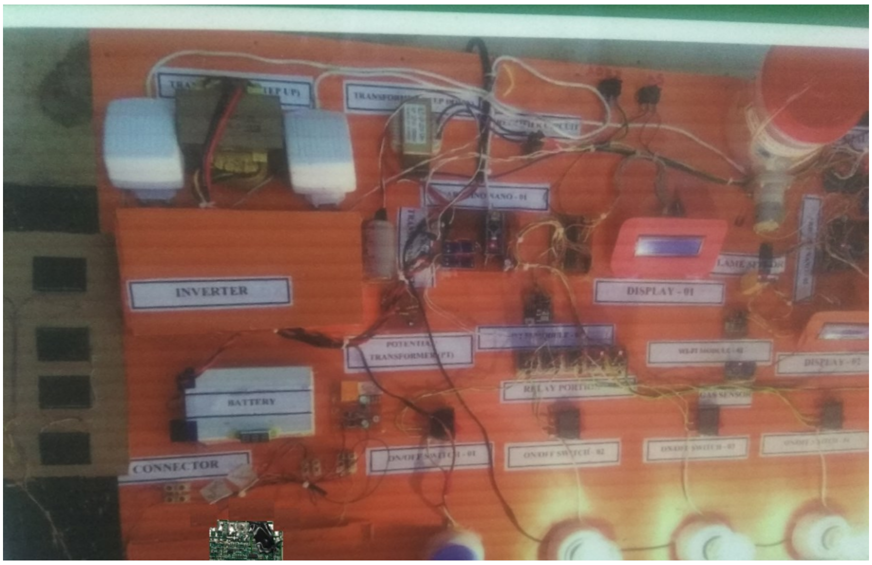

Figure 5: Setup for FLC run by Arduino

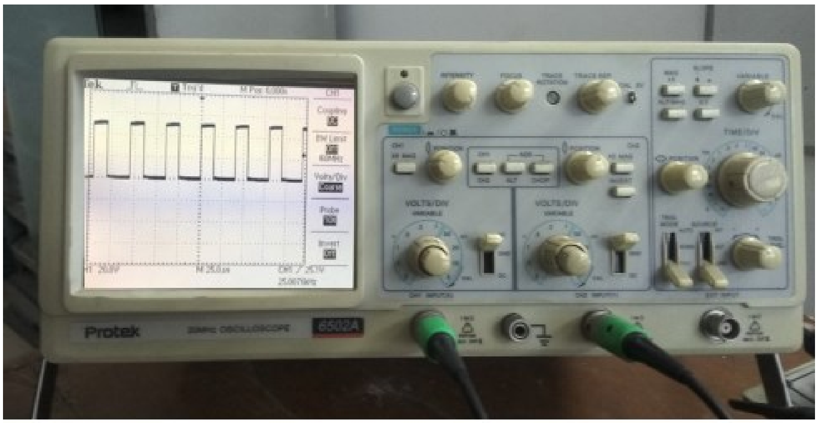

Figure 6: Experimental duty cycle output monitoring

By examining the system's behavior, fuzzy control rules may be derived. In order to enhance tracking performance in terms of dynamic responsiveness and resilience, the various operating circumstances are taken into account.

3. RESULT AND DISCUSSION

The tracking procedure begins with a default duty cycle of D=0. Then, based on projected values that have previously been entered into the fuzzy (1000w/m2, 800w/m2, 600w/m2, 400w/m2, 200w/m2) system, the converter input current Im and voltage Vm are monitored and sensed to determine the duty cycle that can deliver the converter's maximum power output at that moment. This process is repeated repeatedly until the power reaches its maximum and the system stabilizes.

During the simulation, solar irradiation of 1000 W/m2 and a temperature of 25 °C were used to test the two controllers. The outcomes for the power given to the battery with a simulation time of 0.03 s are shown in Figure 7. As can be observed, the two controllers achieve an excellent stability time of 0.005 s and a maximum power extraction of 65 W. Figure 7 shows that, in contrast to the fuzzy control, which is stabilized at a value of D = 0.693, the duty cycle of the P&O control exhibits modest fluctuations between 0.6926 and 0.7.

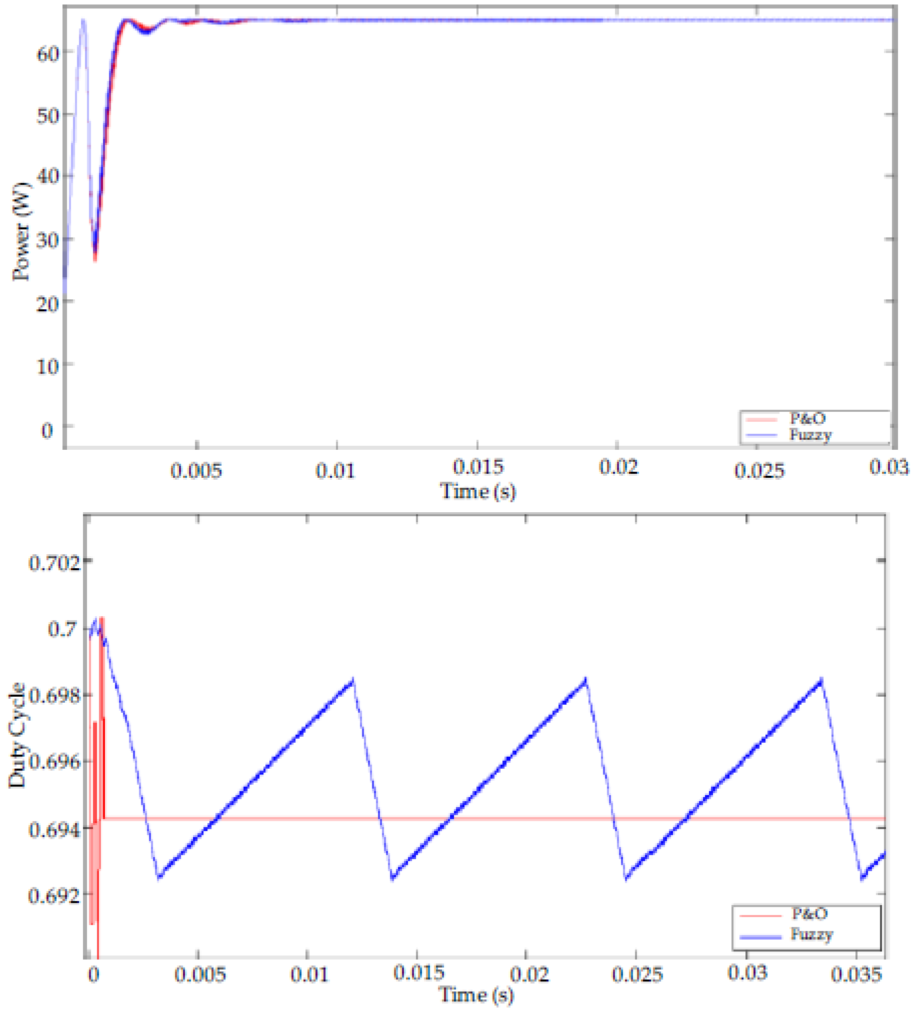

Figure 7: PV system output with the duty cycle

In the second scenario, a 25 °C working temperature and abrupt fluctuations in sun irradiation were used to assess the controllers' effectiveness. At first, an irradiance signal with 200 W/m2 increments between 200 W/m2 and 1000 W/m2 was employed. Irradiance changes occurred every 0.2 seconds during the course of a 1-second simulation.

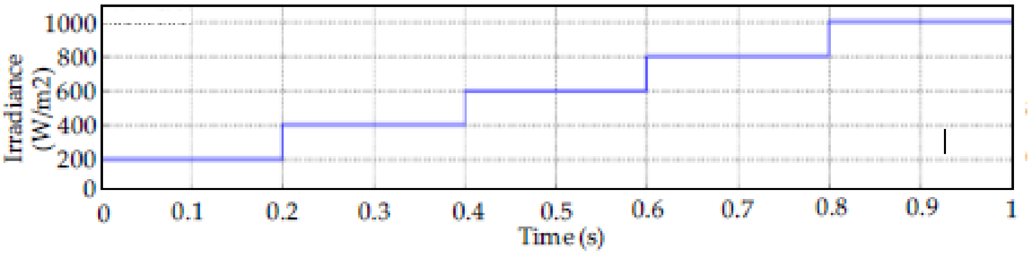

Figure 8: PV system input irradiance with an increment

The test signal used after that had solar irradiance drops between 1000 W/m2 and 200 W/m2 (Figure 8). The output power for irradiance signal increases is shown in Figure 9. Overall, it can be said that the two controllers exhibit satisfactory performance at various moments. The power obtained falls within the duty cycle range of 11.7 W to 64.9 W.

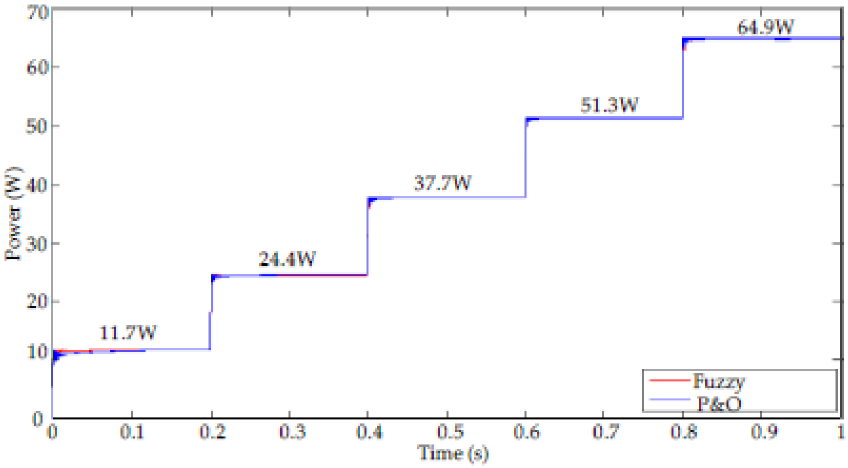

Figure 9: PV system input irradiance with an increment

At this time, constant solar irradiation of 1000 W/m2 was used to assess the system's performance for rapid temperature variations. The signal in Figure 10 was first employed with temperature rises occurring with a difference of 0.2 seconds between 0 to 100 C and the test duration of 1 s. All two controllers function well with an output system power between 63.9 W to 11.6 W, just like with the increased signal. It can be observed that while the P&O system controller exhibits the change that defines this methodology, the system's performance is not adversely impacted.

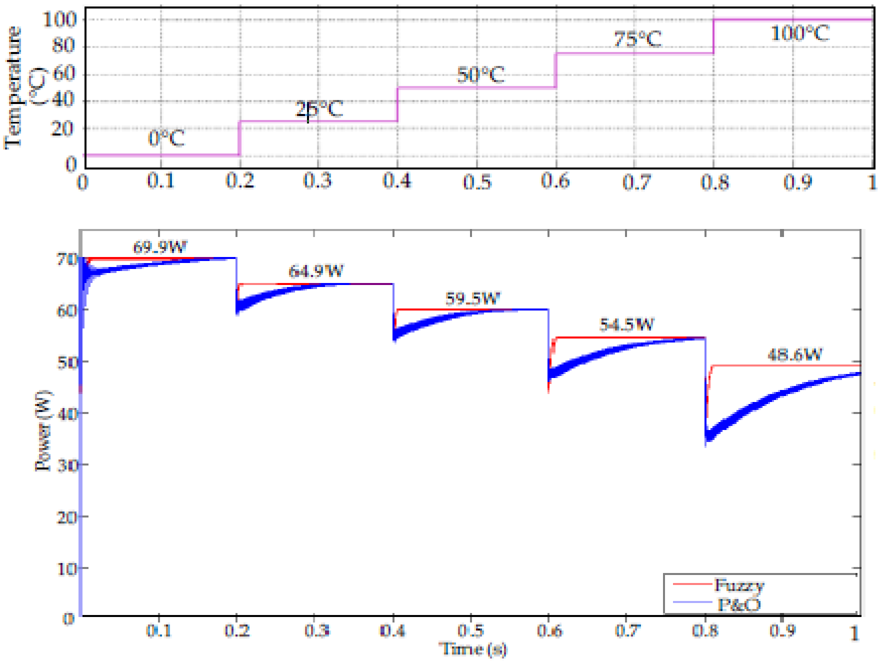

Figure 10: PV system input temperature/output power with an increment

Finally, as seen in Figure 11, the system's performance was assessed for rapid temperature changes and solar irradiation at different values of time ranging from zero to one sec. Figure 11 displays the power collected from Grid-connected PV modules adding fuzzy or P&O system controllers under the stated test conditions. The results show that the FL system controller adheres to the MPP tracking without oscillations or losses. On the other hand, the P&O system controller displays some power losses along with oscillations in reaction to solar irradiation and temperature change. The case studies for the P&O system control that is worst among 0.3 and 0.4 s, during which time the power changes in between 11.5 and 37.5 W when the temperature change counted from 50 to 75 C along with solar irradiation of near about 1000 W/m2.

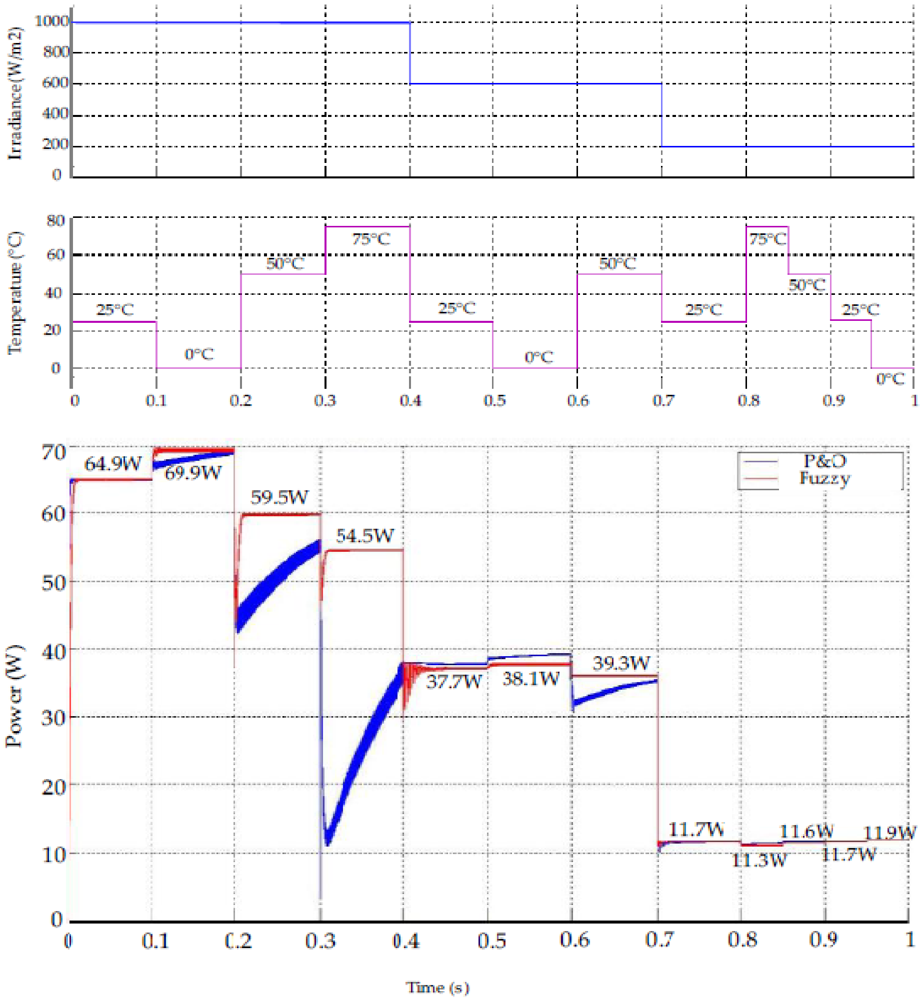

Figure 11: Power Output change due to temperature and irradiance change

The PV module with the highest power point tracking and the performance of the FLC controller and the P&O controller were evaluated. Each part of the Grid-connected PV system is modeled with a MATLAB/Simulink. Alternate test scenarios with changes in temperature along with solar irradiance were analyzed to measure the operation of the Grid connected PV system. It has been checked that the FLC controller functions superbly in these conditions, compared with P&O system control, which is greatly influenced by rapid alteration in the operational temperature of the Grid-connected PV module.

4. CONCLUSION

To conclude the article, a fuzzy logic algorithm is used to control the tracking of the maximum power point of a PV module cell. Finally, the simulated performance was compared with that of a controller run by the P&O algorithm. Here, the PV system with FLC was simulated in Simulink to analyze the performance of the Grid connected system, considering the various test conditions with fluctuation of signals for temperature change and change of irradiation variables of solar power. Compared to P&O logic control, if the system is severely harmed, the fuzzy controller shows excellent performance when the change in temperature for PV operation in the module abruptly. While it was demonstrated that the two controllers worked fine in the existence of differences in solar irradiance and collected the optimum power in accordance with the required electrical system characteristics of the PV module, in comparison, the P&O system controller still displayed regular oscillations. At the same time, there was a sudden change in irradiance. The final consideration for the article is the main contribution of this study, an assurance of fuzzy controller supplied grid-connected PV system power with the maximum amount of electricity possible. Additionally, the fuzzy logic controller is implemented on the inexpensive Arduino platform, demonstrating the advantage of fuzzy control's ease of programming with microcontrollers.

REFERENCES

[1] Karami, N.; Moubayed, N.; Outbib, R. General review and classification of different MPPT Techniques.Renew. Sustain. Energy Rev. 2017, 68, 1–18.

[2] Mohapatra, A.; Nayak, B.; Das, P.; Mohanty, K.B. A review on MPPT techniques of PV system under partial shading condition. Renew. Sustain. Energy Rev. 2017, 80, 854–867.

[3] S. M. Salam, M. I. Uddin and M. R. Bin Moinuddin, "Impact Analysis of Large Number of Non-Linear Lighting Loads on Power Quality in Distribution Network," 2019 4th International Conference on Electrical Information and Communication Technology (EICT), 2019, pp. 1-5, doi: 10.1109/EICT48899.2019.9068811.

[4] Bianconi, E.; Calvente, J.; Giral, R.; Mamarelis, E.; Petrone, G.; Ramos, C.A.; Spagnuolo, G.; Vitelli, M. Perturb and Observe MPPT algorithm with a current controller based on the sliding mode. Int. J. Electr. Power 2013, 44, 346–356.

[5] Chen, M.; Ma, S.; Wu, J.; Huang, L. Analysis of MPPT Failure and Development of an Augmented Nonlinear Controller for MPPT of Photovoltaic Systems under Partial Shading Conditions. Appl. Sci. 2017, 7, 95.

[6] Kwan, T.H.;Wu, X. High performance P&O based lock-on mechanism MPPT algorithm with smooth tracking. Sol. Energy 2017, 155, 816–828.

[7] Alik, R.; Jusoh, A. Modified Perturb and Observe (P&O) with checking algorithm under various solar irradiation. Sol. Energy 2017, 148, 128–139.

[8] S. M. Salam and N. Mohammad, "Load Flow Analysis of a Six Bus System for a Bulk Scale Replacement of Conventional Lighting Loads in a Distributed Network," 2020 IEEE Region 10 Symposium (TENSYMP), 2020, pp. 831-834, doi: 10.1109/TENSYMP50017.2020.9230818.

[9] Cortajarena, J.A.; Barambones, O.; Alkorta, P.; De Marcos, J. Sliding mode control of grid-tied single-phase inverter in a photovoltaic MPPT application. Sol. Energy 2017, 155, 793–804.

[10] Tobón, A.; Peláez-Restrepo, J.; Villegas-Ceballos, J.P.; Serna-Garcés, S.I.; Herrera, J.; Ibeas, A. Maximum Power Point Tracking of Photovoltaic Panels by Using Improved Pattern Search Methods. Energies 2017, 10, 1316.

[11] Loukriz, A.; Haddadi, M.; Messalti, S. Simulation and experimental design of a new advanced variable step size Incremental Conductance MPPT algorithm for PV systems. ISA Trans. 2016, 62, 30–38.

[12] S. M. Salam, M. J. Uddin and S. Hannan, "A new approach to develop a template based load model that can dynamically adopt different types of non-linear loads," 2017 International Conference on Electrical, Computer and Communication Engineering (ECCE), 2017, pp. 708-712, doi: 10.1109/ECACE.2017.7912996.

[13] Hassan, S.Z.; Li, H.; Kamal, T.; Arifo˘ glu, U.; Mumtaz, S.; Khan, L. Neuro-Fuzzy Wavelet Based Adaptive MPPT Algorithm for Photovoltaic Systems. Energies 2017, 10, 394.

[14] Nabipour, M.; Razaz, M.; Seifossadat, S.; Mortazavi, S. A new MPPT scheme based on a novel fuzzy approach.Renew. Sustain. Energy Rev. 2017, 74, 1147–1169.

[15] Majid Dehghani, Mohammad Taghipour, Gevork B. Gharehpetian, and Mehrdad Abedi; Optimized Fuzzy Controller for MPPT of Grid-connected PV Systems in Rapidly Changing Atmospheric Conditions; Journal of modern power systems and clean energy, vol. 9, no. 2, March 2021

ASIAN JOURNAL OF ELECTRICAL AND ELECTRONIC ENGINEERING
Vol. 2 No. 2 2022
E-ISSN: 2785-8189

Performance Analysis of a Newly Designed DC to DC Buck-Boost Converter

M. Iftekher Uddin*, Kazi Samira Shamsi Huq, S M Salam

Dept of EEE, Chittagong University of Engineering and Technology,
Pahartali Rd, Raozan, Chittagong 4349, Bangladesh

*Corresponding author: iftekher28eee@gmail.com

(Received: 1st September 2022; Accepted: 13th September 2022)

Abstract—Most of the electronic devices operate on the principle of the voltage-controlled voltage source. With the improved technology and an increase in circuit complexity, the necessity of controlling the output voltage level irrespective of the change in the load current or line voltage is increasing at a tremendous rate. Moreover, battery dominated electronic devices and gadgets demand a wide range of variation and control over DC voltage and power, which currently faces many challenges. This study proposes a design of a DC to DC Buck-Boost converter and analyzes the converter's performance by placing the Pulse Width Modulation of 40% and 48% duty cycles for buck-mode and 66% and 100% for boost-mode in the switching circuit. The result is simulated in the Proteus Suite software.

Keywords: *Pulse Width Modulation (PWM), Metal Oxide Semiconductor Field Effect Transistor (MOSFET), Switched Mode Power Supply (SMPS), System on a Chip (SoC).*

1. INTRODUCTION

Under the progressive growth of wireless appliances, the demand for low supply voltage is rising. Consumer electronics such as laptop computers and personal communication devices require the lowest possible power supply voltage while maintaining computational throughput and quality of service. Moreover, the terminal voltage of the (NiMH, NiCd, and Li-ion) batteries in portable appliances varies according to the state of their charging condition. Therefore, the system designed with a supply voltage of nominal value requires a converter capable of both stepping-up (boost) and stepping-down (buck) [1, 2] the battery voltage. To achieve the requirement of various levels of DC output voltage under changing supply voltage and load current, a Buck-Boost converter with a smaller number of external components and cost effective SOC design is essential [3].

Control of switching power in DC to DC converter is a challenging task. The function of the control circuit in converter topologies is to nullify the effect of load variations, component tolerances, system aging and input source voltage. The invention of power electronic integrated circuits and solid-state switch-mode circuits has made the voltage regulation process cheaper and more efficient compared to pre-semiconductor ages.

The design of a high-performance control system in DC to DC converter is still challenging. However, among the controlling techniques, the technique that uses the duty cycle variation of PWM is considered the most reliable in the DC-DC power switching converter according to linear models [4, 5]. Two factors have made the control technique most effective, for it remains active for the one-half level of the switching frequency and can be implemented in both (voltage and current) modes.

1.1 Theory of Operation

A buck-boost converter essentially combines the function of a buck and a boost converter. In the boost mode, the converter supplies a higher output voltage to the load than the input voltage, whereas buck mode does the opposite. The Buck-Boost converter works on the periodic charging and discharging of the inductor and the capacitor.

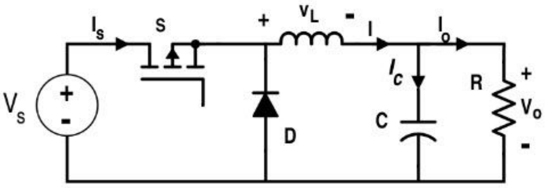

Fig. 1. Schematic of a Buck-Boost Converter

When the switch is on (figure 1), the inductor stores energy from the input in magnetic energy and the capacitor supplies the load. During the off state of the switch, the inductor dissipates its stored energy across R and C. Therefore, the capacitor in the output circuit is assumed to be large enough that the time constant of the RC circuit in the output stage is high. The large time constant compared to the switching period ensures that a constant output voltage V_0 (t) = V_0 exists across load terminals in a steady state.

The switch S is a MOSFET controlled by Pulse Width Modulation (PWM) signal. The main advantage of using a PWM signal in the switching device is the low power loss. In addition, the duty cycle of the PWM signal plays a significant role in the converter's efficiency.

There are two buck-boost converter operation modes based on the PWM signal's switching frequency.

1. Continuous Conduction Mode (CCM)
2. Discontinuous Conduction Mode (DCM)

In CCM, the current through the inductor never goes to zero. Therefore, the inductor partially discharges earlier than the switching cycle. In DCM, the current through the inductor discharges completely at the end of the switching cycle.

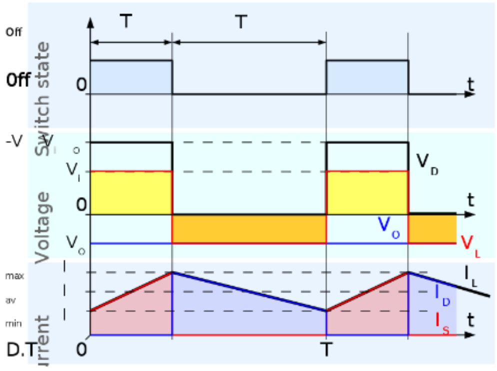

Fig. 2. Converter Operating at Continuous Mode

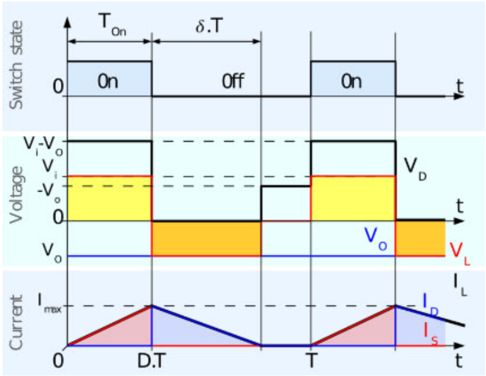

Fig. 3. Converter Operating at Discontinuous Mode

1.2 *Experimental Setup: Block Diagram*

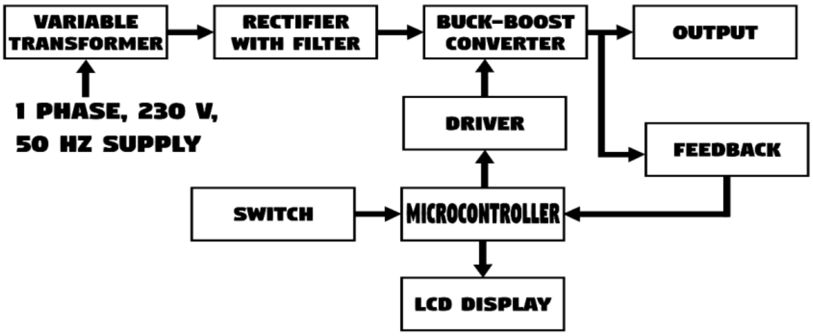

Fig. 4. Block Diagram of the Buck-Boost Converter

1.3 Equipment

Table 1: Parametric Values of the Buck-Boost Converter

Parameter	Value	Parameter	Value
Input inductor	150µH	Load resistance	1Ω
Input capacitor	220µF	MOSFET	IRFP480
Series capacitor with MOSFET	6µF	Microcontroller	PIC16F873
Series resistance with switching circuit	22K	Opto-coupler	TLP-250
Input resistance	22K	Diode	1N4007
Feedback resistance	2K	Switching frequency	31KHz

1.4 Circuit Diagram

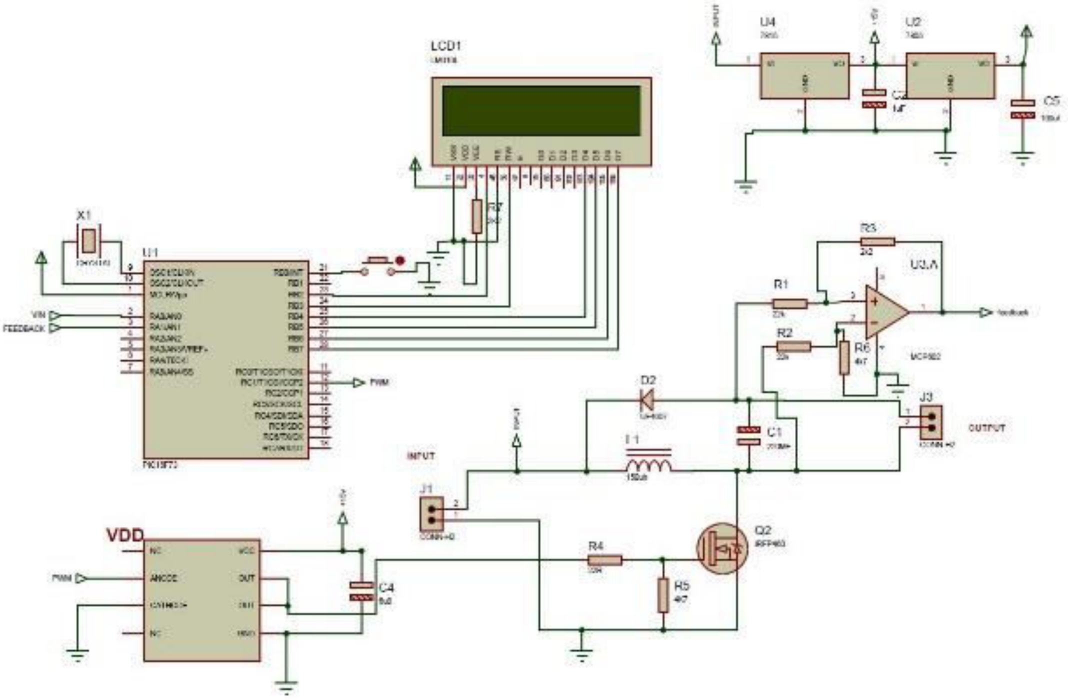

Fig. 5. Circuit Diagram

2. SIMULATION

The circuit simulation in Proteusis performed using the following steps.
i) Configuring Buck-Boost converter circuit on the Proteus software
ii) Simulating the converter circuits under various duty cycles of PWM signal.
iii) Result analysis

2.1 Buck Converter

Table 2: Buck Converter Simulation Data at 48 % and 40% Duty Cycle

Frequency	Period	Capacitance	Inductance	On Time T_{on}	Off Time T_{off}	Duty Cycle	Input Voltage	Output Voltage
31 KHz	32µs	220µF	150µH	12.8µs	19.2 µs	40	29V	25V
				15µs	17 µs	48	25V	24.5V

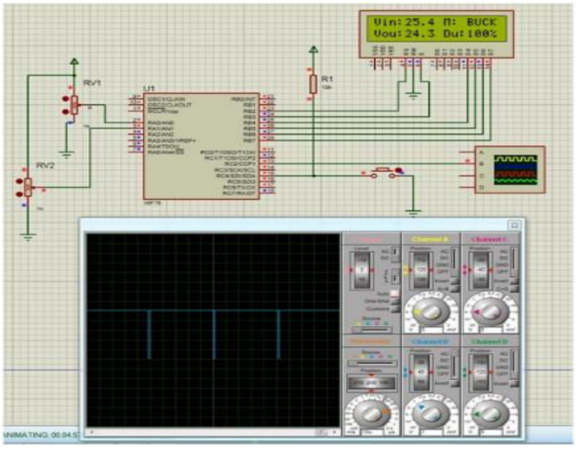

Fig. 6. Buck Mode Simulation with PWM of 48% Duty Cycle

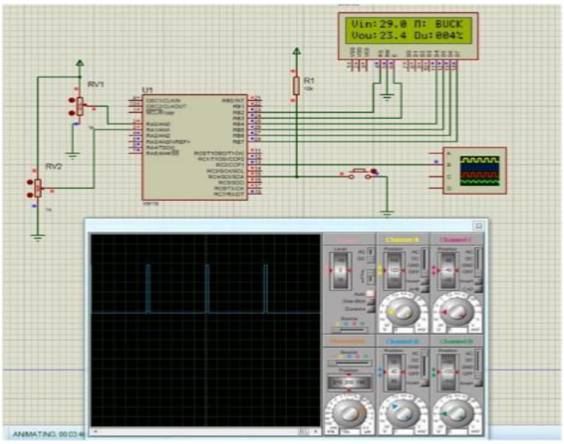

Fig. 7. Simulation of Buck Mode with PWM of 40% Duty Cycle

2.2 *Boost Converter*

Table 3: Boost Converter Simulation Data at 66% and 100% Duty Cycle

Frequency	Period	Capacitance	Inductance	On Time T_{on}	Off Time T_{off}	Duty Cycle	Input Voltage	Output Voltage
31 KHz	32µs	220µF	150µH	21.12 µs	10.88 µs	66%	23 V	25.5 V
				32 µs	0 µs	100%	23.4 V	24.3 V

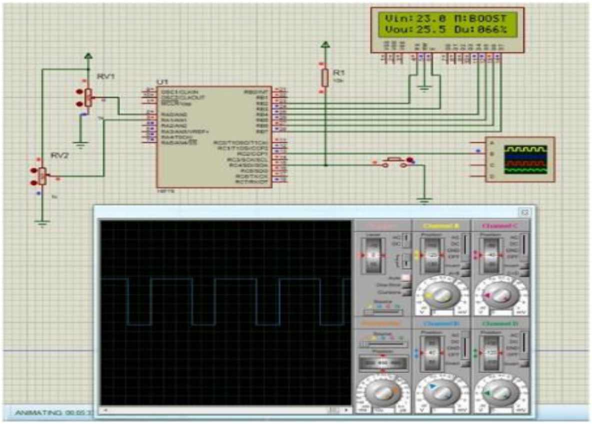

Fig. 8. Boost Mode with PWM of 66% Duty Cycle

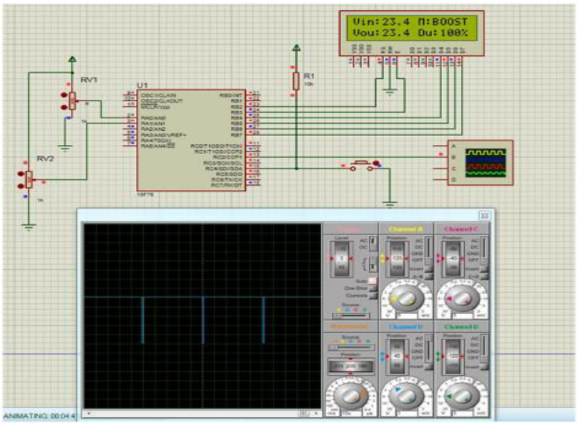

Fig. 9. Boost Mode with PWM of 100% Duty Cycle

For voltage conversion at D = 0.5; where D is the duty cycle of the PWM signal.

Table 4: Converter Simulation Data at 51% Duty Cycle

Parameters	Value
Frequency	31KHz
Period	32 µs
Duty cycle	51%
On Time, T_{on}	16.32µs
Off Time, T_{off}	15. 68µs
Capacitance	220µF
Inductance	150µH
Input voltage	23.4V
Output voltage	23.4V

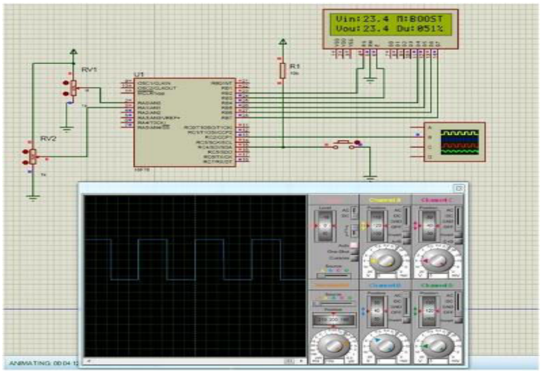

Fig. 10. Converter Operated at PWM of 51% Duty Cycle

2.3 Result Analysis

Table 5: Summary of Result

Modes of Converter	Duty Cycle of PWM	Efficiency
Buck mode	40%	81%
	48%	98%
Boost mode	66%	36%
	100%	0

From the above data table and simulation result, it is evident that in buck mode operation, using$\frac{Output\ Voltage}{Input\ Voltage} = Conversion\ Efficiency = D$, efficiency increases with the increasing percentage of duty cycle up to 50%. For the boost mode of operation, using$\frac{V_{out}-D.V_{out}}{V_{in}} = conversion\ efficiency$, efficiency decreases with the increasing percentage of duty cycle and becomes zero at D = 100% [6, 7, 8]. Obviously, the converter operates at less than 100% duty cycle in boost mode. The primary power losses in a boost converter are mainly due to power switching losses, MOSFET conduction losses and DIODE switching and conduction losses.

3. CONCLUSION

A buck-boost converter provides a wide range of DC voltage and current variation that is optimal for use in modern gadgets and devices. The simplicity of controlling the switching signal's duty cycle has revolutionized the converter's use in digital electronic applications. This study suggests using the converter's Continuous Conduction Mode (CCM) in low voltage, high current applications. In contrast, the Discontinuous Conduction Mode (DCM) is in case of high voltage low current applications. The efficiency in the later is lower, which is not a limiting factor in low power conditions.

REFERENCES

[1] Abdessamad, B, Salah-ddine, K & Mohamed, C 2012, "Designing a High Efficiency Pulse Width Modulation Step-Down DC/DC Converter for Mobile Phone Applications”, IJCSI International Journal of Computer Science Issues, vol. 9, no. 3, viewed 10th March 2020.

[2] Elbakkar, K & Slaoui, K 2011, "Integrated Circuit of CMOS DC-DC Buck Converter with Differential Active Inductor", IJCSI International Journal of Computer Science Issues, vol. 8, no. 6, viewed 10 March 2020.

[3] Langyuan, W & Xiaobo, W 2009, "A Multi-Mode Four-Switch Buck-Boost DC/DC Converter", IEEE Power and Energy Engineering Conference, viewed 10th March 2020.

[4] Erickson, R & Maksimovic, D 2012, Fundamentals of Power Electronics, Springer, New York.

[5] Langyuan, W & Xiaobo, W 2009, "A Multi-Mode Four-Switch Buck-Boost DC/DC Converter", IEEE Power and Energy Engineering Conference, viewed 10th March 2020.

[6] Ngamkong, P, Kochcha, P, Areerak, K, Sujitjorn, S & Areerak, K 2020, "Applications of the generalized state-space averaging method to modelling of DC–DC power converters,", Mathematical and Computer Modelling of Dynamical Systems, vol. 18, no. 3, pp. 243-260, viewed 10th March 2020.

[7] Parvathy, P & Devarajan, N 2012, "Simulation and Implementation of Current-Fed Fullbridge Boost Converter with Zero Current Switching for High Voltage Applications", IJCSI International Journal of Computer Science Issues, vol. 9, no. 3, viewed 10th March 2020.

[8] Simpson, C 2003, Characteristics of Rechargeable Batteries, SNVA533, National Semiconductor, viewed 10th March 2020, <http://www.ti.com/lit/an/snva533/snva533.pdf>.